ELSEVIER

CrossMark

BRACHYTHERAPY

Brachytherapy 15 (2016) 231–239

Physics

Three-dimensional transrectal ultrasound guided high-dose-rate prostate brachytherapy: A comparison of needle segmentation accuracy with two-dimensional image guidance

William Thomas Hrinivich[1,2,*], Douglas A. Hoover[1,3,4], Kathleen Surry[1,3,4], Chandima Edirisinghe[2], Jacques Montreuil[2], David D'Souza[3,4], Aaron Fenster[1,2,3,5], Eugene Wong[1,3,4,5]

[1]*Medical Biophysics, The University of Western Ontario, London, ON, Canada*
[2]*Robarts Imaging Research Laboratories, London, ON, Canada*
[3]*Oncology, University of Western Ontario, London, ON, Canada*
[4]*London Regional Cancer Program, London, ON, Canada*
[5]*Physics and Astronomy, University of Western Ontario, London, ON, Canada*

ABSTRACT

PURPOSE: Conventional transrectal ultrasound guided high-dose-rate prostate brachytherapy (HDR-BT) uses an axially acquired image set for organ segmentation and 2D sagittal images for needle segmentation. Sagittally reconstructed 3D (SR3D) transrectal ultrasound enables both organ and needle segmentation and has the potential to reduce organ-needle alignment uncertainty. This study compares the accuracy of needle tip localization between the conventional 2D sagittally assisted axially reconstructed (SAAR) and SR3D approaches.

METHODS AND MATERIALS: Twelve patients underwent SAAR-guided HDR-BT, during which SR3D images were acquired for subsequent segmentation and analysis. A total of 183 needles were investigated. Needle end-length measurements were taken, providing a gold standard for insertion depths. Dosimetric impact of insertion depth errors (IDEs) on clinical treatment plans was assessed.

RESULTS: SR3D guidance provided statistically significantly smaller IDEs than SAAR guidance with a mean ± SD of -0.6 ± 3.2 mm and 2.8 ± 3.2 mm, respectively ($p < 0.001$). Shadow artifacts were found to obstruct the view of some needle tips in SR3D images either partially (12%) or fully (10%); however, SR3D IDEs had a statistically significantly smaller impact on prostate V_{100}% than SAAR IDEs with mean ± SD decreases of -1.2 ± 1.3% and -6.5 ± 6.7%, respectively ($p < 0.05$).

CONCLUSIONS: SR3D-guided HDR-BT eliminates a source of systematic uncertainty from the SAAR-guided approach, providing decreased IDEs for most needles, leading to a significant decrease in dosimetric uncertainty. Although imaging artifacts can limit the accuracy of tip localization in a subset of needles, we identified a method to mitigate these artifacts for clinical implementation.

Keywords: Prostate cancer; High-dose-rate brachytherapy; 3D ultrasound; Transrectal ultrasound

Introduction

High-dose-rate brachytherapy (HDR-BT) has been shown to be an effective method of dose escalation when used in combination with external beam radiation therapy (EBRT) for the treatment of intermediate- to high-risk prostate cancer (1–4). Clinical trials have shown an improvement in biochemical disease–free survival using HDR-BT dose-escalated EBRT vs. EBRT alone (5, 6). Furthermore, with the recent report of positive results from the ASCENDE-RT randomized trial (7), there will likely be an increase in the number of intermediate-

Received 11 September 2015; received in revised form 9 December 2015; accepted 10 December 2015.

Financial disclosure: This study was supported by the Canadian Institutes of Health Research (CIHR, funding reference number 140352), the Cancer Research and Technology Transfer strategic training program (CaRTT), and the Ontario Institute for Cancer Research (OICR) Imaging Translation program.

* Corresponding author. Room 253, Physics and Astronomy, Western University, 1151 Richmond St., London, ON N6A3K7, Canada. Tel.: +1-519-661-2111x80419; fax: +1-519-661-2033.

E-mail address: whrinivi@uwo.ca (W.T. Hrinivich).

1538-4721/$ - see front matter
http://dx.doi.org/10.1016/j.brachy.2015.12.005

and high-risk prostate cancer patients who will undergo brachytherapy.

Although it is well known that HDR-BT techniques offer improved conformity and normal tissue sparing (8, 9), this presupposes that the needles used to guide the high-activity gamma source have been segmented accurately on imaging, with one study finding that the source must be localized to within 3 mm for acceptable dosimetric uncertainty (10). Because of the high spatial accuracy and high needle-to-tissue contrast in CT imaging, image-guided HDR-BT was originally performed using CT scans acquired after transrectal ultrasound (TRUS)–guided needle insertion (11). Unfortunately, patient repositioning and swelling that occurs during patient setup for CT imaging has been found to cause shifts in needle positions as evidenced by studies reporting mean [range] shifts of 11.5 [0 to 42] mm (12), 10 [5 to 23] mm (13), and 5.4 [−4 to 18] mm (14) between treatment fractions. For patients undergoing single fraction CT-guided HDR-BT, mean shifts of 11 mm have been found between the planning CT and time of treatment delivery, with 10% of needles shifting inferiorly by more than 20 mm (15).

In an effort to eliminate the need to reposition patients during treatment, intraoperative TRUS imaging has been proposed for needle and organ segmentation. By using a tracked probe stepper and compatible segmentation software, TRUS images may be used for needle insertion guidance and segmentation while the patient remains in the operating room. The prostate and nearby organs may be localized by stepping the probe in the superior/inferior direction to create a stack of axial images for segmentation; however, limited image sampling in the needle insertion direction (typically 1–5 mm) introduces uncertainty in needle tip positions (16–18). Siebert *et al.* (16) investigated the ability to identify needle tips in water phantoms and found that submillimeter accuracy was achievable when using the sagittal crystal of a biplane TRUS probe.

With these imaging characteristics in mind, HDR-BT workflows have been proposed that involve segmenting the prostate and nearby organs using an image volume reconstructed from axial images, segmenting needle tips using live 2D sagittal images, and combining the views by manually aligning the axial organ segmentations on a midgland sagittal image, using anatomic landmarks such as the bladder as indicated in Fig. 1. Schmid *et al.* (17) investigated the accuracy of this 2D sagittally assisted axially reconstructed (SAAR) approach in phantoms by comparing TRUS- and CT-based segmentations, finding tip localization accuracy within 1.9 mm is achievable in phantoms with up to 18 needles. Batchelar *et al.* (18) investigated the accuracy of the TRUS-based approach *in vivo* by comparing SAAR-guided needle segmentations with in-room cone-beam CT-based needle segmentations from 37 HDR-BT procedures. Relative needle segmentation error was measured by selecting a posterior needle tip on both the SAAR-guided segmentation and the cone-beam CT-based segmentation and aligning the remaining needle

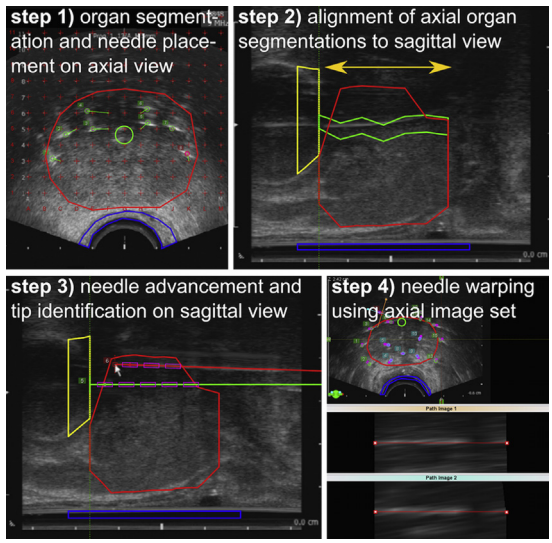

Fig. 1. Screenshots taken from Vitesse treatment planning software during SAAR-guided HDR-BT needle insertion. Major steps of the imaging and segmentation procedure are highlighted, and details are provided in Appendix 1. Among the differences between the SAAR and SR3D-guided segmentation techniques described in this study, the SR3D-guided technique would eliminate the need for the axial-to-sagittal segmentation alignment indicated in Step 2. SAAR = sagittally assisted axially reconstructed; HDR-BT = high-dose-rate brachytherapy; SR3D = sagittally reconstructed 3D.

segmentations using this corresponding point. Results indicated relative tip localization error was less than 3 mm in 97% of all needles when using the SAAR technique. Although the relative needle tip localization accuracy for TRUS-guided HDR-BT is promising, potential systematic shifts in tip positions introduced during the axial-to-sagittal image registration step have not been fully investigated and may contribute to absolute needle tip localization uncertainty.

Our laboratory has previously developed TRUS imaging techniques that allow the reconstruction of a 3D image using the sagittal crystal of a biplane probe by rotating the probe using a motor and simultaneously capturing images (19). This method of acquiring sagittally reconstructed 3D (SR3D) images maintains high spatial resolution in the needle insertion direction while providing a complete 3D image for prostate and organ segmentation, thereby eliminating the need to move the probe in the superior/inferior direction for sagittal and axial imaging and eliminating the axial-to-sagittal segmentation alignment step (20). Variants of this SR3D image reconstruction technique have also been made commercially available, including the Twister image acquisition feature available in Variseed 8.0 (Varian Medical Systems Inc., Palo Alto, CA). Our laboratory has also developed a compact mechatronic device designed for SR3D image-guided transperineal needle insertions that enables superior/inferior probe position tracking relative to an external frame of reference (21). Through calibration, the position of each image relative to the insertion template is determined. Tracking this

position enables the use of needle end-length measurements (22) to estimate absolute insertion depth errors (IDEs) in each image as indicated in Fig. 2. The purpose of this study was to compare needle tip localization accuracy between SAAR and SR3D-guided approaches using calibrated end-length measurements as the gold standard and to estimate the dosimetric impact of measured needle IDEs on clinical treatment plans.

Methods and materials

Image acquisition

Twelve intermediate-risk prostate cancer patients underwent HDR-BT using the conventional SAAR-guided technique. The brachytherapy prescription dose of 15 Gy was delivered in a single fraction and after a 2-week break, all patients went on to receive 37.5 Gy of EBRT delivered in 15 daily fractions (5 week total treatment duration) (23). A BK Medical ProFocus 2202 ultrasound system and 8848 biplane transducer (BK Medical, Boston, MA) were used for imaging at 9 MHz and 6.3-cm field of view. Vitesse software (Varian Medical Systems Inc., Palo Alto, CA,) was used for intraoperative SAAR-guided organ and needle segmentation. The probe and HDR-BT template were supported using the compact mechatronic device, which was affixed to the operating table using an RTP 6000 Precision stabilizer (Brachytherapy Services Inc., Fullerton, VA). Before and after needle insertion, sets of contiguous 2D axial images were acquired in 5-mm steps beginning at the bladder and moving toward the prostate apex for SAAR-guided organ segmentations, immediately followed by SR3D images spanning 140° reconstructed from sagittal images acquired at 0.5° angular intervals. Major steps of the intraoperative SAAR workflow are indicated in Fig. 1, and details are included in Appendix 1. All SR3D needle segmentations were performed postoperatively in this study

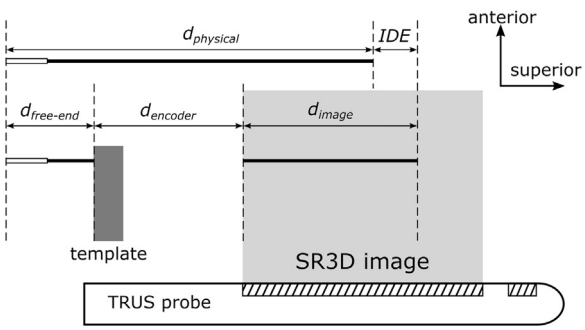

Fig. 2. Schematic of measurements used to calculate needle insertion depth error (IDE). IDE was determined using the physical needle length ($d_{physical}$), needle end-lengths measurements (d_{end}), distance from the template face to the inferior edge of the image volume determined by calibrated encoder positions ($d_{encoder}$), and the length of the image-defined needle (d_{image}). IDE was then calculated as $IDE = (d_{end} + d_{encoder} + d_{image}) - d_{physical}$. SR3D = sagittally reconstructed 3D; TRUS = transrectal ultrasound.

for comparison with the standard clinical SAAR method and were not used for intraoperative treatment planning or delivery. The University of Western Ontario Health Sciences Research Ethics Board approved the use of the device with patients for comparison with conventional image-guided brachytherapy needle insertions.

3D TRUS-guided mechatronic device

The compact mechatronic device for SR3D-guided transperineal needle insertions previously developed in our laboratory (21) was modified to include a manual probe stepper required in the conventional SAAR-guided HDR-BT procedure. An HDR-BT template mounting point and haptic feedback at 5-mm increments were incorporated in the design, similar to the manual stepper regularly used in our clinic (Classic stepper, CIVCO Medical, Coralville, IA). These modifications permitted the acquisition of co-registered axial and SR3D images with minimal disruption to the conventional HDR-BT workflow. An encoder was used to track the superior/inferior probe position, and a string phantom calibration was performed allowing the use of these encoder values to calculate the position of all axial and SR3D images relative to the HDR-BT template face. This calibration procedure is discussed in the Appendix 2, along with estimates of mechanical uncertainty.

Postoperative image segmentation and registration

After the HDR-BT procedure, the SR3D images were imported into BrachyVision (Varian Medical Systems Inc., Palo Alto, CA) for retrospective analysis. To enable comparison of needle segmentations produced using the two imaging techniques, postneedle insertion SR3D images were rigidly registered to the postneedle insertion SAAR axial image sets for each patient as follows. Longitudinal encoder positions recorded for each image along with the sagittal-to-axial crystal distance were used to align the SAAR axial image set and SR3D images in the superior/inferior direction, aligning the anatomic landmarks from both sets. Measurements of these calibrated encoder values are discussed in the Appendix 2. Encoder values corresponding to the axial image set for 1 patient were not recorded, so anatomic landmarks were used to register the axial image set with the SR3D image. The imaged probe cover was used to align the images in the anterior/posterior and left/right directions. Ultrasound machine image lag has previously been found to cause small angular shifts in SR3D images about the probe's axis of rotation (21). These angular rotations were found to be on the order of 2.5° in this study and were manually corrected based on anatomic landmarks.

All needles were manually segmented in BrachyVision as they appeared on the postinsertion SR3D images by a medical physicist (DH). A single midgland axial image from the intraoperative treatment plan was crossreferenced during this retrospective needle segmentation for the sole purpose of assigning identical needle labels between SAAR and SR3D image sets. All data were anonymized and exported from Eclipse as DICOM files for geometric analysis using

MATLAB 2015a (Mathworks, Natick, MA). All statistical tests were performed using SPSS 21 (IBM, Armonk, NY).

Needle tip position comparison between SAAR and SR3D-guided segmentation

Needle tip positions were compared between imaging techniques by bringing both sets of segmentations to a common coordinate system using the transformation matrix produced by the rigid registration. Box plots of tip position differences were produced for each patient individually to determine whether tip differences were distributed evenly among all patients or whether patient-specific differences existed.

Insertion depth comparison between segmentations and physical measurements

Needle insertion depths determined using the two imaging techniques were compared with physical end-length measurements to estimate the absolute IDE as shown schematically in Fig. 2. The length of each segmented needle within the SR3D image was determined, from the needle tip to where the needle exited the SR3D image at the inferior edge (d_{image}). The distance between the inferior edge of the SR3D image and the inferior face of the insertion template on the mechatronic device (d_{encoder}) was calculated based on the encoder positions recorded intraoperatively. The encoder position values were calibrated to give d_{encoder} using the string phantom as discussed in the Appendix 2. From the string phantom measurements, we estimated the uncertainty of d_{encoder} to be ± 0.5 mm. The needle end-lengths (d_{end}) were physically measured intraoperatively using a graduated ruler during the procedure with estimated ± 0.5 mm uncertainty. By comparing this needle length to the physical length of the needle (d_{phys}), an IDE could be estimated, as indicated in Eq. 1.

$$\text{IDE} = \left(d_{\text{end}} + d_{\text{encoder}} + d_{\text{image}}\right) - d_{\text{physical}} \quad (1)$$

This process was performed for all needles using both the intraoperative SAAR-guided segmentations and postoperative SR3D-guided segmentations enabling comparison of IDEs between imaging methods. Insertion depth accuracy was assessed by comparing patient-specific median IDEs, and insertion depth precision was assessed by comparing patient-specific interquartile ranges and full ranges. Patient-specific metrics were compared using Wilcoxon signed-rank tests.

Effect of image artifacts on IDEs

Needles present in TRUS images attenuate ultrasound signal, creating shadow artifacts that may obstruct the view of some of the more anterior needle tips. Because the SR3D needle segmentations were performed using an image acquired after all needles are inserted, we determined the prevalence of needles obstructed by shadow artifacts and their impact on tip localization accuracy. The medical physicist performing the SR3D segmentations was asked to qualitatively classify needle tips as unobstructed, partially obstructed, or obstructed based on needle tip signal intensity relative to background signal intensity. Unobstructed needles were classified as having high apparent needle tip contrast, whereas obstructed needles were those where the needle appeared to enter a signal void, beyond which the trajectory and tip could no longer be identified. Partially obstructed needles were those that could not be clearly categorized as obstructed or unobstructed; typically having low needle tip contrast but without an obvious signal void at the needle tip. A one-way analysis of variance and Tukey's post hoc tests were used to compare IDEs between needle tip appearance groups for the SR3D-guided segmentations.

Dosimetric impact of IDEs

The dosimetric impact of IDEs was determined as follows: Starting with the clinical treatment plan, two new plans were generated per patient in Brachyvision based on the SAAR and SR3D IDEs. The clinical intraoperatively planned dwell positions were shifted in the superior/inferior direction by each needle's IDEs measured for SAAR guidance and for SR3D guidance. The volume of the prostate receiving 100% of the prescription dose (V_{100}%) and volume of the urethra receiving 120% of the prescription dose (V_{120}%) were compared between the clinical and simulated treatment plans for each patient. The mean changes in dosimetric parameters attributed to the SAAR and SR3D-guided IDEs were compared using two-sided paired t tests.

Results

Needle tip position comparison between SAAR and SR3D-guided segmentation

In total, 194 needles were inserted among all 12 patients. Eleven needles were excluded from analysis including three steel needles used during one HDR-BT procedure, two needles that were moved after SR3D image acquisition, five anterior needles that could not be detected in SR3D images from 4 patients, and one needle that appeared to extend beyond the edge of the SR3D image. The five needles that could not be visualized are addressed further in the Discussion. This resulted in 183 needles included in the segmentation analysis. Figure 3 displays 3D renderings of the coregistered needle segmentations of 2 patients intersecting an axial slice of the postinsertion SR3D image. Figure 4a–4c display box plots of the tip distance components individually for each patient and for all patients combined. In terms of Euclidean distance, the position of the needle tips identified using the two imaging methods differed by less than 3 mm in 33% of the cases and by less than 5 mm in 64% of the cases. The largest difference components were noted to be in the superior/inferior direction.

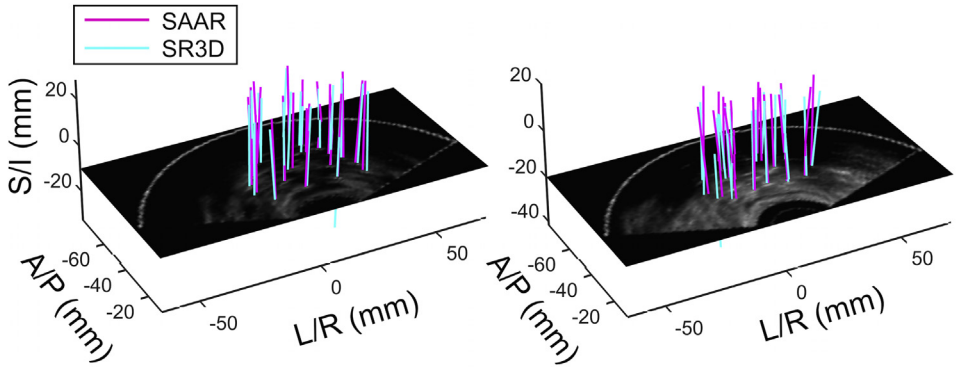

Fig. 3. 3D renderings of the coregistered needle segmentations produced using SAAR and SR3D-guided needle segmentation approaches of 2 patients as an indication of needle density in the region of interest. Needle renderings are shown intersecting axial views of the SR3D images for each patient. SAAR = sagittally assisted axially reconstructed; SR3D = sagittally reconstructed 3D.

Insertion depth comparison between segmentations and physical measurements

Figure 4d and 4e show box plots of the IDEs determined by the SAAR and SR3D-guided approaches individually for each patient and summarized over all patients. Mean ± SD values of IDEs over all 183 needles were found to be 2.8 ± 3.2 mm and −0.6 ± 3.2 mm for the SAAR and SR3D-guided approaches, respectively. This difference was found to be statistically significant ($p < 0.001$). The box plots indicate statistically significantly larger systematic errors in the SAAR vs. SR3D-guided approach, with patient-specific median value ranges of (−1.1 mm, 6.4 mm) vs. (−2.1 mm, 3.7 mm), respectively ($p < 0.01$). The box plots also indicate statistically significantly larger patient-specific interquartile ranges determined using the SAAR-guided approach with interpatient ranges of (1.3 mm, 5.9 mm) vs. (0.8 mm, 2.2 mm) determined with the SR3D-guided approach ($p < 0.01$). Examining the maximum IDEs by looking at the full range of patient-specific needle IDEs (indicated by the maximum and minimum dots for each patient), there was no statistical difference between the SR3D-guided and the SAAR-guided approach, with median values of 9.8 mm and 8.3 mm, respectively ($p > 0.05$).

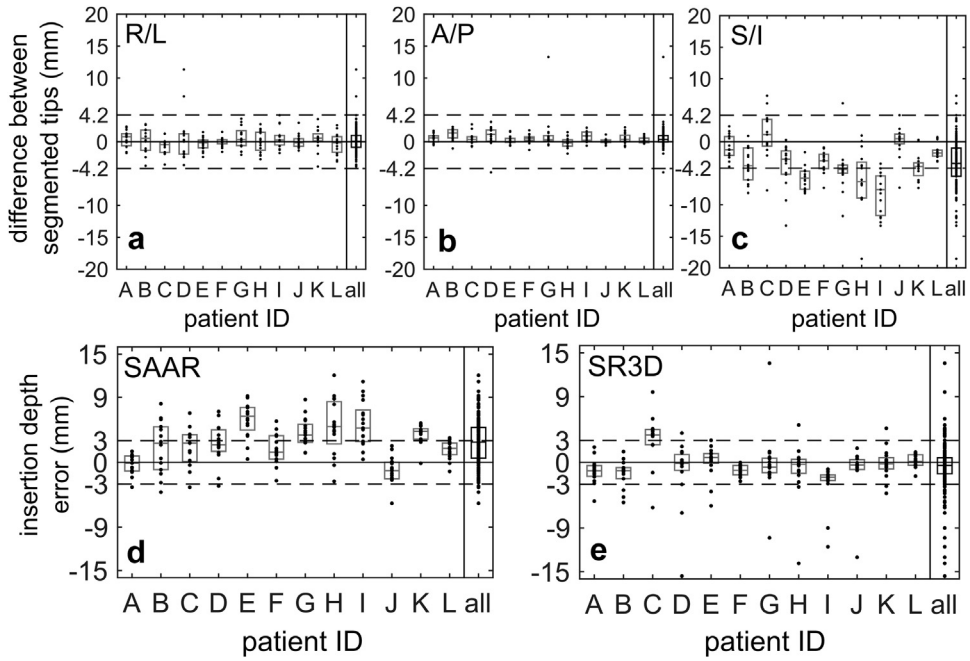

Fig. 4. (a–c) Plots of components of the differences between needle tips identified using the SAAR and SR3D-guided needle segmentation approaches. In (a–c), *horizontal lines* indicate difference thresholds of ±4.2 mm, which are obtained by adding the ±3 mm error threshold for each segmentation method in quadrature. This difference threshold was indicated for each difference component for visual comparison. (d–e) Plots of insertion depth errors estimated from needle end-length measurements for needles tips identified using SAAR and SR3D-guided needle segmentation approaches. The data are plotted separately for each patient and for all 12 patients combined. In (a–e), *boxes* indicate interquartile range and *center lines* indicate median value. SAAR = sagittally assisted axially reconstructed; SR3D = sagittally reconstructed 3D.

Effect of image artifacts on IDEs

Figure 5 shows a box plot of IDEs from all 183 needles segmented using the SR3D-guided approaches and grouped based on the tip appearance on the SR3D image. Table 1 summarizes mean IDEs for each group displayed in Fig. 5. Seventy-eight percent of needles were considered unobstructed, 12% were considered partially obstructed, and 10% were considered obstructed. Over all 183 needles analyzed, the SR3D-guided approaches provided IDEs of ±3 mm for 83% of needles and ±5 mm for 92% of needles. Within the unobstructed group, the SR3D-guided approach provided IDEs within ±3 mm for 91% of needles and ±5 mm for 98% of needles; however, needle tip appearance on the SR3D image was not found to have a statistically significant effect on mean IDE based on a one-way analysis of variance ($p > 0.05$).

Dosimetric impact of IDEs

Dosimetric parameters corresponding to the intraoperatively produced treatment plans are listed in Table 2, along with the changes in parameters associated with the IDEs from the SAAR and SR3D-guided needle segmentation approaches, indicated by ΔSAAR and ΔSR3D, respectively.

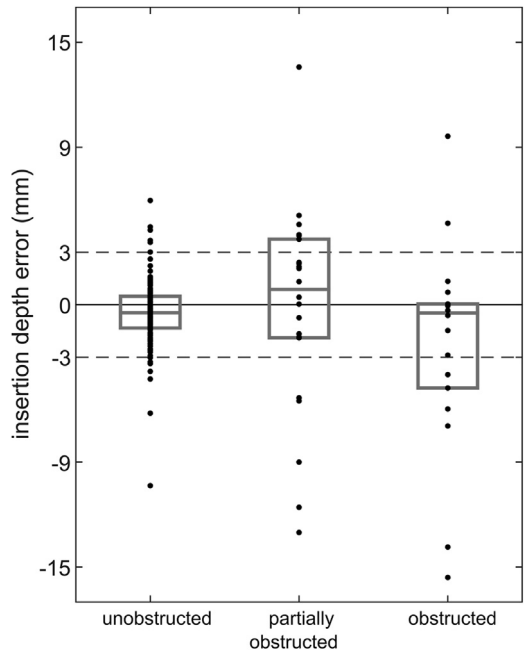

Fig. 5. Plot of insertion depth errors estimated from needle end-length measurements for needles from all 12 patients using SR3D-guided needle segmentation. Needles were qualitatively classified as "unobstructed," "partially obstructed," or "obstructed" based on needle tip intensity relative to background intensity on the SR3D images to determine the prevalence and impact of the ultrasound shadow artifacts on insertion depth error. Seventy-eight percent of needle tips appeared unobstructed, 12% appeared partially obstructed, and 10% appeared obstructed. *Boxes* indicate interquartile range, and *center lines* indicate median value. SR3D = sagittally reconstructed 3D.

Table 1
Needle tip appearance and insertion depth errors determined using SR3D-guided segmentation

	Unobstructed	Partially obstructed	Obstructed	All
Number (percentage) of needles	143 (78)	22 (12)	18 (10)	183 (100)
Mean (SD) insertion depth error (mm)	−0.47 (1.84)	−0.22 (5.98)	−2.23 (5.92)	−0.63 (3.22)

SR3D = sagittally reconstructed 3D.

In terms of target coverage, the SAAR-guided IDEs tended to produce greater decreases in prostate V_{100}% than the SR3D-guided IDEs with mean ± SD of −6.5 ± 6.7% and −1.2 ± 1.3%, respectively. This difference was found to be statistically significant ($p < 0.01$). In the SR3D-guided case, prostate V_{100}% decreases of less than 3% were found in 11 of 12 patients, and decreases of less than 5% were found in all patients. Loss of target coverage in the SAAR-guided case tended to occur at the prostate base attributed to systematic superior shifts in SAAR-imaging identified needle tips. Changes in urethral dose due to both the SAAR and SR3D-guided IDEs depended on patient anatomy. Mean ± SD changes in urethra V_{120}% were found to be −2.1 ± 6.6% and −0.2 ± 3.8% for the SAAR and SR3D-guided IDEs, respectively, but this difference was not found to be statistically significant ($p > 0.05$).

Discussion

The focus of this study was to compare needle tip localization accuracy of SAAR and SR3D-guided HDR-BT. Our results indicate that the SR3D-guided approach provides more accurate and precise insertion depths than the SAAR-guided approach for most needles, leading to improvements in prostate V_{100}%. Both techniques rely on the sagittal transducer for tip identification. The observed decrease in systematic errors in the SR3D-guided segmentations is attributed to eliminating the need to move the probe in the superior/inferior direction for axial image acquisition after needle tip identification with the sagittal ultrasound crystal, thereby mitigating organ motion and eliminating the axial-to-sagittal alignment step necessary in the SAAR procedure. By eliminating the dependence on axial image stacks for organ segmentation, the SR3D-guided procedure could replace the clinical SAAR-guided procedure by making use of the preneedle and postneedle insertion SR3D images for organ segmentation. After the preinsertion SR3D image acquisition, the live 2D axial view may be used to monitor initial needle insertions to ensure midgland coverage, but would not be necessary otherwise. SR3D image acquisition takes less than 15 seconds, and the images have been shown to enable prostate

Table 2
Dosimetric impact of needle insertion depth errors

	Prostate V_{100}%			Urethra V_{120}%		
Patient	Intraoperative, %	ΔSAAR, %	ΔSR3D, %	Intraoperative, %	ΔSAAR, %	ΔSR3D, %
A	97.1	0.6	0.6	1.8	−0.6	0.3
B	97.0	−2.8	−1.1	2.3	−1.3	1.9
C	91.5	−1.5	−4.0	19.1	−6.9	7.0
D	95.9	−9.6	−2.7	8.3	−7.2	−7.2
E	92.2	−13.5	−0.8	29.5	−19.3	−6.7
F	96.1	−3.0	0.5	9.2	7.0	−2.1
G	95.3	−6.7	−1.5	0.0	0.0	0.0
H	95.6	−21.8	−1.6	0.0	0.0	0.0
I	96.2	−11.0	−1.1	0.0	0.0	1.4
J	93.9	−0.3	−2.2	1.8	−0.2	−0.7
K	96.6	−8.3	−0.7	0.0	1.3	2.5
L	96.6	−0.7	0.1	0.1	2.3	0.8
Mean	95.3	−6.5	−1.2	6.0	−2.1	−0.2
SD	1.8	6.7	1.3	9.4	6.6	3.8

SAAR = sagittally assisted axially reconstructed; SR3D = sagittally reconstructed 3D.

segmentations with intraoperator variability on the order of 1 mm (24). This procedure may improve overall segmentation accuracy while improving efficiency over conventional methods. Furthermore, the increased superior/inferior spatial resolution of the SR3D images may ease needle segmentation quality assurance, which currently must be performed using an axial image stack.

Although this study did find advantages in SR3D over SAAR in terms of decreases in systematic IDE, we identified a limitation of the method: a single postneedle insertion SR3D image volume is prone to shadow artifacts created by posterior needles. The impact of these artifacts is evidenced by the five needles (3%) that needed to be excluded from analysis due to the inability to be detected, and the 10% of needles appearing obstructed in the SR3D images. We have shown that a user may manually detect a subset of unobstructed needles with IDEs within 3 mm for 91% of needles. Our center is currently evaluating needle tip segmentation on live 2D sagittal images, which may be automatically transferred to the SR3D image coordinate system based on the current probe angle. This tool would provide the benefits of the live sagittal needle tip identification step, including the ability to identify tips working anteriorly to posteriorly and incorporating the dynamic information of the live 2D view, while still eliminating the need to move the probe in the superior/inferior direction for final image acquisition. This method will also eliminate the possibility of needles being undetectable or extending beyond the edge of the SR3D image as observed in this study because needles may be repositioned at the time of tip identification to avoid these errors.

The mean ± (standard error of the mean) IDE of 2.8 ± 0.2 mm corresponding to the SAAR-guided needle segmentation approach indicates a systematic shift of needle segmentations superior to the actual needle tip location within the axial image set. All needle tips are positioned relative to the final axial image set based on the axial-to-sagittal alignment step, which is performed using anatomic landmarks. It is possible that systematic errors in the axial-to-sagittal alignment are introduced by anatomic shifts caused by the insertion of HDR-BT needles. To assess the direction and degree of anatomic shifts created during the procedure, encoder positions of the preinsertion and postinsertion axial image sets were recorded for the last 8 patients in the study. The postinsertion images were acquired to capture the same anatomic features as the preinsertion images, so the difference in encoder values approximated anatomic shifts introduced between the imaging time points. Encoder values indicated a superior anatomic shift for all 8 patients, with mean ± SD of 12.6 ± 5.4 mm. A superior anatomic shift occurring between axial-to-sagittal alignment step and needle tip identification step may create a superior needle tip shift consistent with the observations in this study; however, further investigation into this effect is required.

A limitation of this study was the dependence on an external frame of reference (the insertion template) for comparison of needle IDEs, when in actuality the needle tip position relative to the superior prostate border is the most critical distance for treatment planning accuracy. We did not investigate this distance in the present study due to a lack of consistent prostate segmentations produced using each imaging method. The external frame of reference allowed the use of the mechatronic device encoders for image and segmentation registration and allowed the use of needle end-length measurements as a gold standard for insertion depths. Before final image acquisition, the needles were locked into place using a set screw on the template to prevent any further movement. The final axial image stack and SR3D volume were acquired consecutively for all patients; however, it is possible that organ motion may have been introduced by moving the probe in the superior/inferior direction to acquire the final axial image stack.

Another limitation of this study was the 5 mm sampling used to acquire the axial image sets for the SAAR-guided segmentations. Previous studies have investigated manual steppers that provide superior/inferior indexing in 1 mm steps in an effort to improve resolution in the sagittal plane (17, 18). Resolution in this plane is fundamentally limited by the elevational resolution of the axial transducer. The transverse aperture of the BK 8848 transducer, which is related to this minimum resolution, is specified as 5.5 mm. Mechanical focusing may create a focal zone with finer elevational resolution; however, Peikari *et al.* (25) showed that this thickness is highly sensitive to distance from the transducer, signal gain, and the presence of side-lobe artifacts produced by aberrant lower frequencies. Although the elevational resolution of the sagittal transducer also limits the axial resolution of the SR3D reconstruction investigated in this study (19), the improved spatial resolution in the sagittal plane while maintaining acceptable resolution in the axial plane enables segmentation of the needles and organs, respectively.

Conclusion

This study compared HDR-BT needle tip location, IDEs, and the dosimetric impact of IDEs on clinical treatment plans between SAAR and SR3D guidance. The mechatronic device used for image acquisition enables the reconstruction of a 3D image by rotating the sagittal crystal, thereby eliminating the need to move the probe in the superior/inferior direction after needle tip identification. With current SAAR approaches, this probe movement must be compensated by performing an axial-to-sagittal registration introducing systematic uncertainty in needle tip location. Through comparison with calibrated needle end-length measurements, we have found that SR3D guidance provides improved needle tip localization accuracy for most needles relative to SAAR guidance, leading to statistically significant improvements in dosimetric uncertainty. Ultrasound artifacts present in postneedle insertion SR3D images may limit segmentation accuracy for a subset of needles, and we have proposed a method to overcome this limitation for clinical implementation. These TRUS-based segmentation techniques also eliminate the need to adjust patient position for CT imaging, thereby decreasing patient discomfort and eliminating the probability of needle shifts occurring before treatment delivery.

Supplementary data

Supplementary data related to this article can be found at http://dx.doi.org/10.1016/j.brachy.2015.12.005.

References

[1] Heidenreich A, Bastian PJ, Bellmunt J, *et al*. EAU guidelines on prostate cancer. Part 1: Screening, diagnosis, and local treatment with curative intent—update 2013. *Eur Urol* 2014;65:124–137.

[2] Hoskin PJ, Colombo A, Henry A, *et al*. GEC/ESTRO recommendations on high dose rate afterloading brachytherapy for localised prostate cancer: An update. *Radiother Oncol* 2013;107:325–332.

[3] Podder TK, Beaulieu L, Caldwell B, *et al*. AAPM and GEC-ESTRO guidelines for image-guided robotic brachytherapy: report of Task Group 192. *Med Phys* 2014;41:101501–101527.

[4] Yamada Y, Rogers L, Demanes DJ, *et al*. American Brachytherapy Society consensus guidelines for high-dose-rate prostate brachytherapy. *Brachytherapy* 2012;11:20–32.

[5] Marina O, Gustafson GS, Kestin LL, *et al*. Comparison of dose-escalated, image-guided radiotherapy vs. dose-escalated, high-dose-rate brachytherapy boost in a modern cohort of intermediate-risk prostate cancer patients. *Brachytherapy* 2014;13:59–67.

[6] Hoskin PJ, Rojas AM, Bownes PJ, *et al*. Randomised trial of external beam radiotherapy alone or combined with high-dose-rate brachytherapy boost for localised prostate cancer. *Radiother Oncol* 2012;103:217–222.

[7] Morris WJ, Tyldesley S, Pai H, *et al*. Low-dose-rate brachytherapy is superior to dose-escalated EBRT for unfavourable risk prostate cancer: the results of the ASCENDE-RT randomized control trial. *Brachytherapy* 2015;14:S12.

[8] Hermesse J, Biver S, Jansen N, *et al*. A dosimetric selectivity intercomparison of HDR brachytherapy, IMRT and helical tomotherapy in prostate cancer radiotherapy. *Strahlenther Onkol* 2009;185:736–742.

[9] Georg D, Hopfgartner J, Gòra J, *et al*. Dosimetric considerations to determine the optimal technique for localized prostate cancer among external photon, proton, or carbon-ion therapy and high-dose-rate or low-dose-rate brachytherapy. *Int J Radiat Oncol Biol Phys* 2014;88:715–722.

[10] Tiong A, Bydder S, Ebert M, *et al*. A small tolerance for catheter displacement in high–dose rate prostate brachytherapy is necessary and feasible. *Int J Radiat Oncol Biol Phys* 2010;76:1066–1072.

[11] Kolotas C, Baltas D, Zamboglou N. CT-based interstitial HDR brachytherapy. *Strahlenther Onkol* 1999;175:419–427.

[12] Hoskin PJ, Bownes PJ, Ostler P, *et al*. High dose rate afterloading brachytherapy for prostate cancer: Catheter and gland movement between fractions. *Radiother Oncol* 2003;68:285–288.

[13] Mullokandov E, Gejerman G. Analysis of serial CT scans to assess template and catheter movement in prostate HDR brachytherapy. *Int J Radiat Oncol Biol Phys* 2004;58:1063–1071.

[14] Kim Y, Hsu IC, Pouliot J. Measurement of craniocaudal catheter displacement between fractions in computed tomography-based high dose rate brachytherapy of prostate cancer. *J Appl Clin Med Phys* 2007;8:2415–2427.

[15] Holly R, Morton GC, Sankreacha R, *et al*. Use of cone-beam imaging to correct for catheter displacement in high dose-rate prostate brachytherapy. *Brachytherapy* 2011;10:299–305.

[16] Siebert FA, Hirt M, Niehoff P, Kovács G. Imaging of implant needles for real-time HDR-brachytherapy prostate treatment using biplane ultrasound transducers. *Med Phys* 2009;36:3406–3412.

[17] Schmid M, Crook JM, Batchelar D, *et al*. A phantom study to assess accuracy of needle identification in real-time planning of ultrasound-guided high-dose-rate prostate implants. *Brachytherapy* 2013;12:56–64.

[18] Batchelar D, Gaztañaga M, Schmid M, *et al*. Validation study of ultrasound-based high-dose-rate prostate brachytherapy planning compared with CT-based planning. *Brachytherapy* 2014;13:75–79.

[19] Tong S, Downey DB, Cardinal HN, Fenster A. A three-dimensional ultrasound prostate imaging system. *Ultrasound Med Biol* 1996;22:735–746.

[20] Fenster A, Downey DB, Cardinal HN. Three-dimensional ultrasound imaging. *Phys Med Biol* 2001;46:R67–R99.

[21] Bax J, Smith D, Bartha L, *et al*. A compact mechatronic system for 3D ultrasound guided prostate interventions. *Med Phys* 2011;38: 1055–1069.

[22] Damore SJ, Syed AMN, Puthawala AA, Sharma A. Needle displacement during HDR brachytherapy in the treatment of prostate cancer. *Int J Radiat Oncol Biol Phys* 2000;46:1205–1211.

[23] Helou J, D'Alimonte L, Loblaw A, *et al*. High dose-rate brachytherapy boost for intermediate risk prostate cancer: Long-term outcomes of two different treatment schedules and early biochemical predictors of success. *Radiother Oncol* 2015;115:84–89.

[24] Hu N, Downey DB, Fenster A, Ladak HM. Prostate boundary segmentation from 3D ultrasound images. *Med Phys* 2003;30:1648–1659.

[25] Peikari M, Chen TK, Lasso A, *et al*. Characterization of ultrasound elevation beamwidth artifacts for prostate brachytherapy needle insertion. *Med Phys* 2012;39:246–256.

PATIENT QA, MACHINE QA, DEVICES AND DATA — ALL IN ONE PLACE

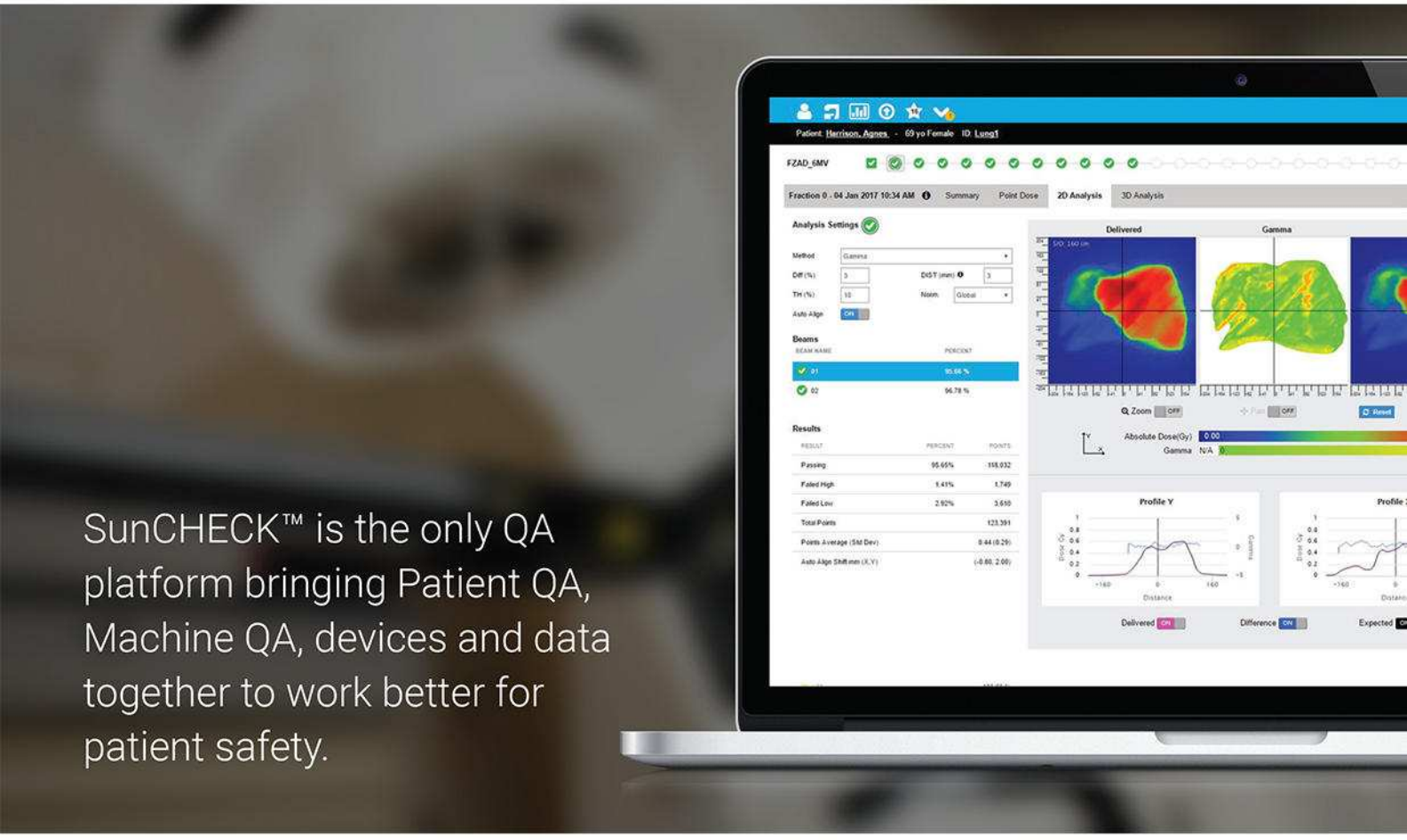

SunCHECK™

With a single interface and a single database, SunCHECK will cover:

- Dose**CHECK**™ - Independent secondary 3D dose calculations
- Per**FRACTION™ Fraction 0™** - Phantom-less 2D and 3D pre-treatment QA
- Per**FRACTION™ Fraction n™** - 3D transit/in-vivo monitoring
- SNC **Machine™** - TG-142/VMAT imaging and mechanical QA
- SNC **Routine™** - Daily, monthly and annual test management, with live device integration COMING SOON

This is precisely the kind of QA innovation you can always expect from Sun. Innovations that help improve outcomes and workflow efficiency, with ease.

sunnuclear.com

SUN NUCLEAR corporation

Simultaneous automatic segmentation of multiple needles using 3D ultrasound for high-dose-rate prostate brachytherapy

William Thomas Hrinivich[a)]
Department of Medical Biophysics, University of Western Ontario, London, Ontario N6A 5C1, Canada
Imaging Research Laboratories, Robarts Research Institute, University of Western Ontario, London, Ontario N6A 5K8, Canada

Douglas A. Hoover and Kathleen Surry
Department of Medical Biophysics, University of Western Ontario, London, Ontario N6A 5C1, Canada
Department of Oncology, University of Western Ontario, London, Ontario N6A 4L6, Canada
London Regional Cancer Program, London, Ontario N6A 5W9, Canada

Chandima Edirisinghe and Jacques Montreuil
Imaging Research Laboratories, Robarts Research Institute, University of Western Ontario, London, Ontario N6A 5K8, Canada

David D'Souza
Department of Oncology, University of Western Ontario, London, Ontario N6A 4L6, Canada
London Regional Cancer Program, London, Ontario N6A 5W9, Canada

Aaron Fenster
Department of Medical Biophysics, University of Western Ontario, London, Ontario N6A 5C1, Canada
Department of Oncology, University of Western Ontario, London, Ontario N6A 4L6, Canada
Department of Physics and Astronomy, University of Western Ontario, London, Ontario N6A 3K7, Canada
Imaging Research Laboratories, Robarts Research Institute, University of Western Ontario, London, Ontario N6A 5K8, Canada

Eugene Wong
Department of Medical Biophysics, University of Western Ontario, London, Ontario N6A 5C1, Canada
Department of Oncology, University of Western Ontario, London, Ontario N6A 4L6, Canada
Department of Physics and Astronomy, University of Western Ontario, London, Ontario N6A 3K7, Canada
London Regional Cancer Program, London, Ontario N6A 5W9, Canada

(Received 19 July 2016; revised 10 January 2017; accepted for publication 29 January 2017; published 14 March 2017)

Purpose: Sagittally reconstructed 3D (SR3D) ultrasound imaging shows promise for improved needle localization for high-dose-rate prostate brachytherapy (HDR-BT); however, needles must be manually segmented intraoperatively while the patient is anesthetized to create a treatment plan. The purpose of this article was to describe and validate an automatic needle segmentation algorithm designed for HDR-BT, specifically capable of simultaneously segmenting all needles in an HDR-BT implant using a single SR3D image with ~5 mm interneedle spacing.

Materials and Methods: The segmentation algorithm involves regularized feature point classification and line trajectory identification based on the randomized 3D Hough transform modified to handle multiple straight needles in a single image simultaneously. Needle tips are identified based on peaks in the derivative of the signal intensity profile along the needle trajectory. For algorithm validation, 12 prostate cancer patients underwent HDR-BT during which SR3D images were acquired with all needles in place. Needles present in each of the 12 images were segmented manually, providing a gold standard for comparison, and using the algorithm. Tip errors were assessed in terms of the 3D Euclidean distance between needle tips, and trajectory error was assessed in terms of 2D distance in the axial plane and angular deviation between trajectories.

Results: In total, 190 needles were investigated. Mean execution time of the algorithm was 11.0 s per patient, or 0.7 s per needle. The algorithm identified 82% and 85% of needle tips with 3D errors ≤3 mm and ≤5 mm, respectively, 91% of needle trajectories with 2D errors in the axial plane ≤3 mm, and 83% of needle trajectories with angular errors ≤3°. The largest tip error component was in the needle insertion direction.

Conclusions: Previous work has indicated HDR-BT needles may be manually segmented using SR3D images with insertion depth errors ≤3 mm and ≤5 mm for 83% and 92% of needles, respectively. The algorithm shows promise for reducing the time required for the segmentation of straight HDR-BT needles, and future work involves improving needle tip localization performance through improved image quality and modeling curvilinear trajectories. [https://doi.org/10.1002/mp.12148]

Key words: 3D ultrasound, high-dose-rate brachytherapy, needle segmentation, prostate brachytherapy, randomized Hough transform

1. INTRODUCTION

High-dose-rate prostate brachytherapy (HDR-BT) dose distributions are critically sensitive to uncertainty in radiation source positions relative to the prostate and surrounding organs, which in turn depend on uncertainty in needle positioning.[1–3] For this reason, modern intraoperatively planned HDR-BT involves imaging needles in their final positions to localize trajectories and tips relative to anatomy.[4] Intraoperative imaging was originally performed using CT,[5] but patient repositioning required for CT acquisition was found to cause mean needle shifts of 11 mm between imaging and treatment delivery, and shifts of >20 mm in 10% of needles.[6] MRI-guided HDR-BT insertions have been proposed, but require patient repositioning for treatment[7,8] or modified MRI suites for in-bore treatment.[9,10] Transrectal ultrasound (TRUS)-guided HDR-BT techniques have been developed, enabling the segmentation of needles using multiple live 2D sagittal images and volumetric segmentation of organs using contiguous sets of axial images,[11] thereby eliminating the need for patient repositioning between imaging and treatment.[12,13] We recently completed a study investigating 3D TRUS-guided HDR-BT based on robotic sagittally reconstructed 3D (SR3D) images,[14] which are acquired by rotating the probe using a motor while simultaneously tracking probe position and acquiring sagittal images in a fan geometry.[15,16] This method of image reconstruction mitigates tip localization uncertainty by eliminating the need to switch between sagittal and axial transducers or move the probe in the superior/inferior direction.[14] Increasing needle and organ segmentation accuracy remains a primary objective in HDR-BT imaging, but all imaging and segmentation must be performed intraoperatively, typically while the patient is under general anesthesia, adding a time constraint to the procedure. As we have demonstrated that HDR-BT needles may be manually segmented accurately on a static SR3D image, an automatic HDR-BT needle segmentation algorithm may further decrease overall treatment time.

A number of investigators have proposed line detection algorithms for the segmentation of single needles in 3D ultrasound images *in vivo* showing promising performance for specific needle-guidance tasks.[17–31] Techniques have been proposed based on orthogonal projections;[17,18] geometric transformations such as parallel integral projections (PIP),[19] the 3D Hough transform (3DHT),[20–26] and the generalized Radon transform;[27–29] and iterative methods such as random sample consensus (RANSAC).[30,31] These techniques have all been validated using image regions containing single needles; however, the algorithm requirements for HDR-BT needle segmentation, as discussed by Buzurovic et al.,[32] have not been fully investigated. HDR-BT procedures involve multiple needles inserted through a rigid template placed on the perineum. Typical spacing between adjacent template holes is 5 mm, and needle and probe deflection between the template and imaged region can lead to uncertainty in needle placement greater than this spacing.[33] This uncertainty makes extrapolation from calibrated template hole positions infeasible for trajectory identification or subvolume cropping to isolate regions containing individual needles, making existing algorithms unsuitable for HDR-BT needle segmentation.

The purpose of this study was to expand upon previous work by describing a needle segmentation algorithm designed for SR3D images containing multiple needles based on a version of the randomized 3DHT with additional regularization steps. The segmentation algorithm is validated using SR3D images from 12 prostate cancer patients who underwent HDR-BT including 190 needles. Algorithm-based segmentation results are compared geometrically to manual segmentation results, and the impact of SR3D image artifacts on algorithm performance is investigated.

2. METHODS

2.A. Image acquisition and segmentation

Twelve intermediate-risk prostate cancer patients underwent conventional sagittally assisted axially reconstructed (SAAR) ultrasound-guided HDR-BT using a compact mechatronic device to support the ultrasound probe and insertion template,[16] enabling the acquisition of SR3D images of the prostate with all needles inserted. The imaging study was approved by the University of Western Ontario Health Sciences research ethics board. A Profocus 2202 ultrasound machine and 8848 bi-planar TRUS probe (BK Medical, Peabody MA, USA) operating at 9 MHz and 6.3 cm imaging depth were used for image acquisition. Sagittal images were acquired over 140° at 0.5° angular intervals, resulting in images with size $870 \times 441 \times 408$ and $0.16 \times 0.16 \times 0.16$ mm^3 reconstructed voxel dimensions. SR3D image spatial resolution varies with distance from the probe, with the highest spatial resolution component in the direction parallel to the transducer (z), and the lowest spatial resolution component in the reconstructed direction tangential to the direction of probe rotation (t). The device calibration and HDR-BT workflow have been described previously.[14] Following the procedure, a medical physicist manually segmented and labeled all needles present in the SR3D images using Brachyvision treatment planning software (Varian Medical Systems, Palo Alto CA, USA). The needle segmentations produced intraoperatively using SAAR-guidance were used for treatment planning and delivery, and were referenced during the manual SR3D segmentation procedure to ensure that each needle was labeled correctly. We limited our consideration to straight needle detection; however, in cases where needles appeared to bend, only the needle tip and most inferior observable point along the trajectory were selected to approximate a linear best-fit. These manual linear SR3D segmentations were then used as the "gold standard" for validation of the segmentation algorithm.

The algorithm was used to segment all needles present in the SR3D images. The algorithm was implemented in MATLAB 2015a (MathWorks, Natick MA, USA) on a

desktop PC running Windows 10 (Microsoft, Redmond WA, USA) with a 3.4 GHz Core i7-3770 CPU (Intel, Santa Clara CA, USA), 16 GB of RAM, and a GeForce GTX 660 graphics card (NVIDIA, Santa Clara CA, USA) with 2 GB of memory. As input, the algorithm required the postinsertion SR3D image and the number of needles inserted. Needle labeling also required manually identified axial needle intersection points to create correspondences between template hole labels and automatically identified trajectories. The execution times of each major algorithm component were recorded for each patient.

2.B. Segmentation algorithm

Major steps of the algorithm are outlined in Fig. 1. The five major assumptions of the algorithm are (a) needles appear brighter in the image than the local background, (b) all needles enter the image from the inferior edge, (c) needle trajectories are within 10° of being normal to the axial plane, (d) needle trajectories are separated from one another by ≥3 mm in the axial plane and therefore do not cross, and (e) for a given patient, all needles will have insertion depths within the range [−12 mm, 10 mm] relative to the median insertion depth for that patient. It should be noted that clinical practice may vary, leading to violations of assumptions (c)–(e); however, these parameter limits reflected our institutional practice and experience. Specific parameter limits were selected based on geometric analysis of the manual segmentations, provided in Appendix A. Major algorithm components are described in further detail in the following sections.

2.B.1. Image filtering

A convolution filter was applied to the SR3D images based on the method proposed by Perona and Malik[34] designed to enhance edges with the same width as the needle cross-section. The image is convolved with the second partial derivative of a Gaussian distribution with the same width as the expected edge width. The primary needle insertion component is in the superior direction, so needles appear as edges in directions along the axial plane. The two primary spatial resolution components in the axial plane of the SR3D image are radial (r) and tangential (t) to the axis of probe rotation, corresponding to the axial and elevational resolution components of the sagittal transducer. The elevational spatial resolution is lower than the axial spatial resolution,[35] resulting in the needles appearing "smeared" along the t direction as shown in Fig. 2(a). To account for this smearing, SR3D images were transformed to r, t coordinates as shown in Fig. 2(c), and two 3D convolution kernels were applied corresponding to second partial derivatives in the r and t directions, respectively. The z component of both kernels was a uniform distribution, and the r and t directions were second partial derivatives of a 2D Gaussian distribution ($\Phi(r,t)$) with standard deviations of 0.4 mm and 1.2 mm, matching the typical r and t components of an axial needle cross-section as shown in Figs. 2(d)–2(e). The kernels had (r, t, z) dimensions of $2.4 \times 4.8 \times 10.0$ mm^3, and were applied in 0.16 mm steps in the r and t directions and 2 mm steps in the z direction. The results of the two convolutions were combined in quadrature to produce the final filtered signal intensities. The filter can be expressed as

$$I_{filtered}(r,t,z) = \sqrt{\sum_{i=1,2}\left(\frac{\partial^2}{\partial x_i^2}\Phi(r,t,z) \otimes I_{raw}(r,t,z)\right)^2} \quad (1)$$

where I_{raw} and $I_{filtered}$ are the unfiltered and filtered signal intensities, x_1 and x_2 are r and t directions, Φ is the convolution kernel, and $\otimes$ represents the convolution. Although SR3D image spatial resolution varies with distance from the probe (r), the convolution kernel dimensions were kept constant throughout the entire image.

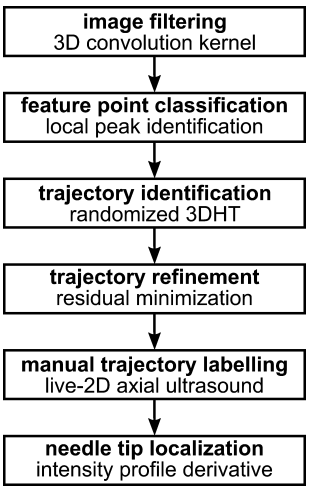

FIG. 1. Flowchart indicating the major steps of the segmentation algorithm.

2.B.2. Feature point classification

In order to isolate the centers of intensity peaks as needle feature points while minimizing the inclusion of additional surrounding points, local intensity peaks were identified in each axial slice while enforcing a minimum distance in the axial plane of 3 mm between adjacent peaks. First, an intensity threshold was selected as the 98th percentile of the filtered image intensity values, and was applied to generate a set of candidate feature points. Next, pairs of candidate feature points with separation distance in the axial plane <3 mm were compared, and the voxel with the lowest signal intensity was eliminated. This regularization step was parallelized and executed using a GPU.

2.B.3. Trajectory identification

Needle trajectories were identified using the randomized 3DHT, similar to the method described by Qiu et al.[21] extended to distinguish feature points corresponding to multiple needles. The method involves randomly selecting pairs of

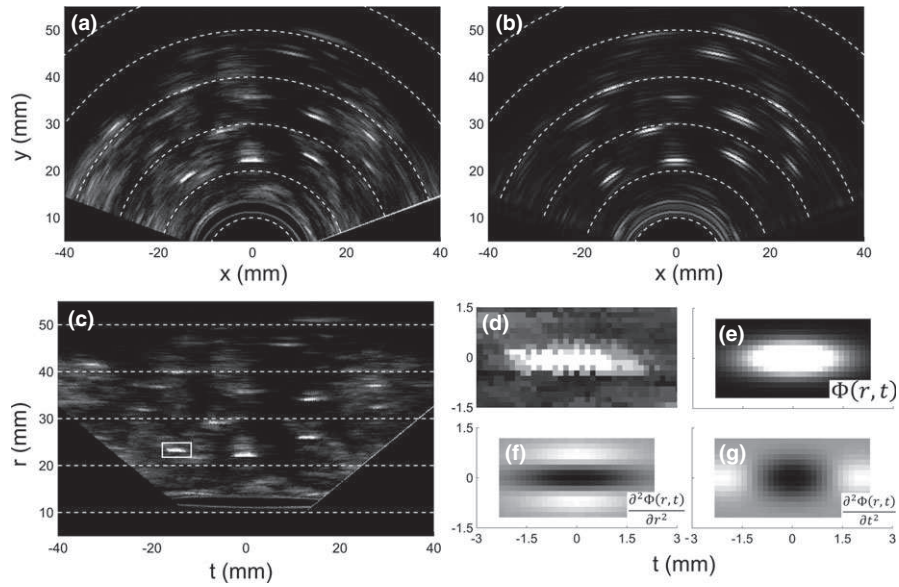

FIG. 2. (a-b) Example axial slice from an SR3D image before and after filtering. (c) The unfiltered axial slice from (a) transformed to the radial-tangential (r, t) coordinate system. Dotted grid-lines in a–c) indicate the t direction in the image. (d) Magnified view of the needle intersection point indicated by the white box in c). (e) 2D Gaussian distribution with standard deviations in the r and t directions of 0.4 mm and 1.2 mm. (f–g) Second partial derivatives of the 2D Gaussian distributions in the r and t directions.

feature points, calculating the parameters of the line in 3D space that those feature points define, and indexing an accumulator using those parameters. For our application, we chose the point-orientation representation, which defines the line's orientation using the azimuthal and elevational angles (ϕ, θ), and the line's position using a point along the line, specifically the coordinates of the line's intersection point with a 2D axial plane (x_{int}, y_{int}) at the inferior image face defined as $z = 0$. This parameterization is sufficient to characterize all possible lines which intersect the inferior plane of the image volume using the ordered 4-tuple $(\phi, \theta, x_{int}, y_{int})$.

Given a randomly selected pair of feature points $p_1[x_1, y_1, z_1]$ and $p_2[x_2, y_2, z_2]$, a unit vector in the direction of the line defined by these points was calculated as $\hat{b} = (p_2 - p_1)/|p_2 - p_1|$. A minimum distance threshold of 10 mm in the z direction was applied to point pairs to exclude highly oblique orientations, and $\hat{b}$ was multiplied by the sign of the b_z component to ensure that $\hat{b}$ was oriented in the positive$z$ direction. The ordered 4-tuple (ϕ, θ, x_{int}, y_{int}) describing the line can be calculated according to Eqs. 2–5.

$$\phi = tan^{-1}\left(\frac{b_x}{b_y}\right) \tag{2}$$

$$\theta = tan^{-1}\left(\frac{b_z}{\sqrt{b_x^2 + b_y^2}}\right) \tag{3}$$

$$x_{int} = x_1 - b_x z_1 \tag{4}$$

$$y_{int} = y_1 - b_y z_1 \tag{5}$$

The azimuthal angle ϕ could take any value from [–180°, 180°], but the elevational angle was limited to the range [0°, 10°] from the z-axis. The x_{int} and y_{int} parameter values were limited to ranges of [−40 mm, 40 mm] and [10 mm, 60 mm], encompassing the area occupied by the template hole range used for all 12 patients plus lateral and anterior margins of 15 mm. Any lines with parameters outside of these limits were not entered in the accumulator. To index the accumulator, ϕ and θ were binned at 1° angular intervals and x_{int} and y_{int} were binned at 1-mm intervals. At these intervals, the 4D accumulator had a size of 360 × 11 × 81 × 51. Random point pair selection and accumulator indexing were parallelized and executed using the GPU, employing a constant 10^8 point pairs for each patient.

All feature points representing all lines in the 3D image were used as input in the 3DHT, leading to multiple accumulator peaks corresponding to multiple lines. The point-orientation line representation enabled the direct interpretation of the parameters x_{int} and y_{int} in terms of the image coordinate system, which could then be used to enforce a minimum distance in the axial plane between lines when identifying these peaks. This was accomplished by first only considering the x_{int} and y_{int} accumulator components, and identifying any local peaks with index values that were greater than an empirically selected threshold of 0.02% of the total number of random point pairs chosen. Next, local peaks were refined by comparing pairs of peak values with separation distance in the axial plane <3 mm and only retaining peaks with the greater index value; identical to the method used for axial feature point regularization. For each of the peaks identified using the x_{int} and y_{int} accumulator components, the corresponding ϕ and θ values were extracted as a secondary 2D accumulator, and the ϕ and θ values with the highest index were selected to define the line's orientation.

2.B.4. Trajectory refinement

Trajectory orientations were refined using the method described by Qiu et al. as outlined in Fig. 3. Feature points within 2 mm of each trajectory were identified, and the line that minimized the sum of the squared residuals with that set of feature points was determined by solving a set of derivative equations.[24] The trajectory identification step tended to identify a greater number of needle-like features than the true number of needles present in the image. To refine the set of candidate trajectories, the trajectories were sorted in descending order based on the number of feature points within 2 mm. Only the $1.5n$ trajectories with the greatest number of feature points were retained, where n was the number of needles physically inserted for that patient.

2.B.5. Manual trajectory labeling

As the needle labeling step of the HDR-BT procedure is critical for treatment delivery, needles are inserted individually while monitoring a live 2D axial view of the prostate mid-gland. The dynamic view of each needle entering the image allows a user to reliably label each needle at the point of intersection with this axial slice. These intraoperatively identified intersection points were used to label the final set of needle trajectories identified by the algorithm as outlined in Fig. 3. For this study, the manual label points were extracted from the SAAR needle segmentations produced intraoperatively, which were labeled using the live 2D axial view as described. 2D points were taken from a mid-gland axial slice of the SAAR segmentations, and these manual label points were transferred to the SR3D image based on a rigid registration calculated using mechatronic device encoder positions. The intersection points of the candidate needle trajectories with the same axial slice were found, and the distances between each manual label point and candidate trajectory were calculated. Each candidate trajectory was labeled according to the nearest manual label point only if the manual label point was within 5 mm of the trajectory, ensuring that each label was only assigned to a single trajectory. Trajectories that were not labeled were discarded, and labels without a trajectory identified within 5 mm were reported as segmentation failures. This labeling procedure resulted in a final set of $\leq n$ trajectories, where n was the number of needles physically inserted for that patient.

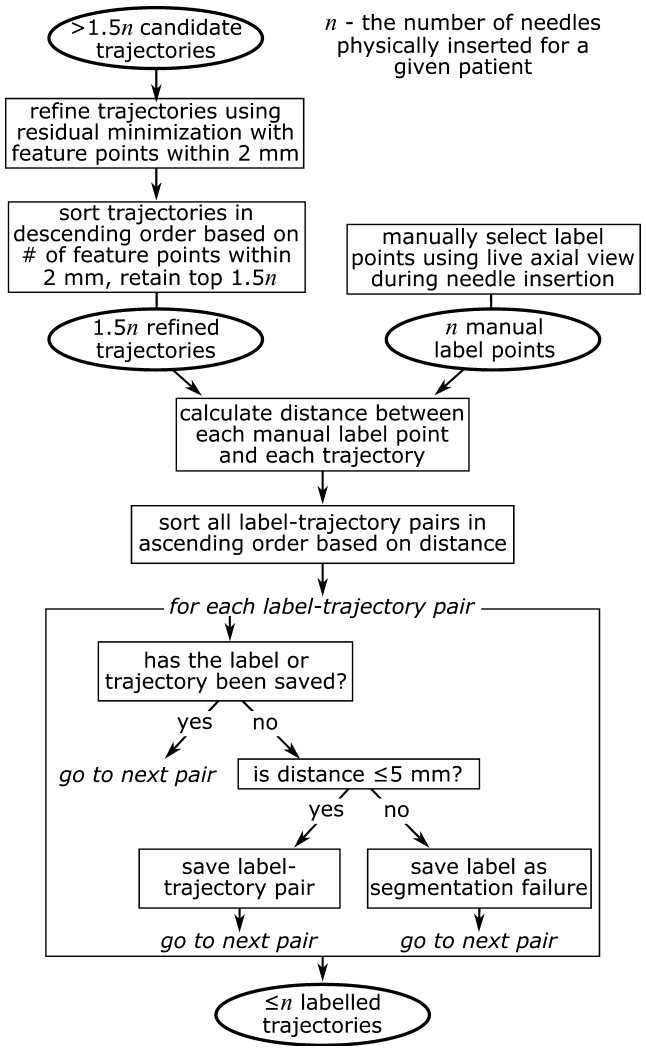

FIG. 3. Process diagram of the trajectory refinement and manual label assignment steps. The input candidate trajectories were identified using the randomized 3DHT.

2.B.6. Needle tip localization

Needle tip positions were determined using a two-step procedure based on the signal intensity profile along each needle trajectory and the practice of inserting needles to the prostate–bladder interface, limiting the range of insertion depths expected for each patient. First, drops in signal intensity corresponding to the needle tip were identified based on peaks in the derivative of the signal intensity profile as indicated in Fig. 4. This involved cropping and filtering a small subvolume oriented along each trajectory, then averaging intensity values normal to the trajectory to create a 1D intensity profile. The derivative of this profile was calculated and normalized by the maximum value. Peaks in the normalized derivative profile with values greater than a threshold of 0.7 were identified, and the needle tip was selected as the most superior of these peaks. The insertion depth of each needle was calculated as the distance along the trajectory from the inferior image edge to the identified tip. Details of the oriented subvolume cropping, subvolume filtering, and signal intensity profile analysis are provided in Appendix section B.

Next, the median value of these insertion depths was calculated, and a valid insertion depth search space was limited to the range [−12 mm, 10 mm] relative to this median value. The tip identification procedure was repeated for all needles over this limited search space to identify the final tip positions. The selection of these asymmetric search space limits was based on the observed insertion depth ranges of manual segmentations, provided in Appendix section A.

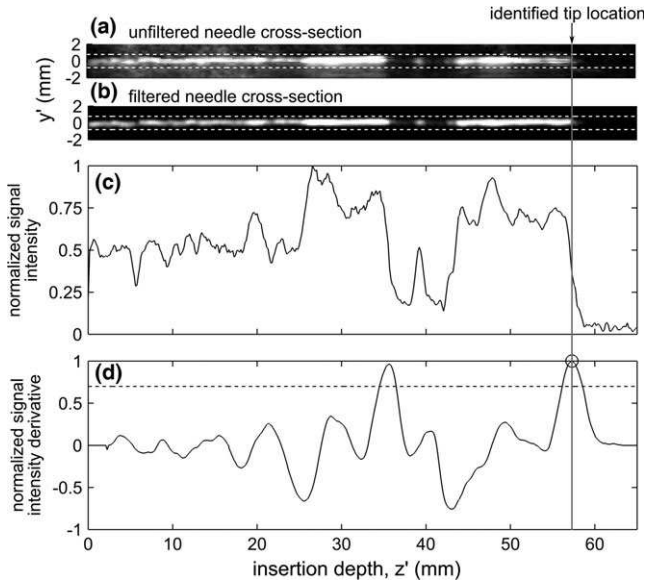

FIG. 4. (a-b) Example cropped needle cross-section expressed in local line coordinates before and after filtering. The horizontal white dotted lines in (a-b) indicate the y' cropping limits used to create the 1D signal intensity profile. (c) Normalized 1D signal intensity profile. (d) Normalized signal intensity derivative profile. The horizontal dotted line indicates the derivative threshold used for selecting the tip location, which is indicated by the vertical gray line.

2.C. Segmentation accuracy

2.C.1. Trajectory localization accuracy

Needle trajectories identified by the algorithm were compared with manual segmentations in terms of location and orientation. Let $p_m[p_{m,x}, p_{m,y}]$ and $p_a[p_{a,x}, p_{a,y}]$ be the 2D intersection points of the manual and algorithm-based segmentations with the inferior SR3D image face, respectively. The trajectory location errors were characterized in terms of the 2D Euclidean distance in the axial plane $|\vec{d}_{traj}|$, where $\vec{d}_{traj} = p_a - p_m$. This definition was chosen as $\vec{d}_{traj}$ is independent of needle insertion depth, and is the farthest point along the needle from the tip while remaining within the SR3D image. $\vec{d}_{traj}$ components were expressed in terms of r and t components at the point p_m. The rotation matrix used to calculate these components is described in Appendix C. Principal component analysis was used to determine the primary directions of trajectory error variance and 95% prediction interval ellipses (ellipse containing 95% of the points).[36,37]

Let $\hat{b}_m$ and $\hat{b}_a$ be unit vectors pointing in the directions of the manual and algorithm-based segmentations, respectively. Angular trajectory errors were defined as the angle α between $\hat{b}_m$ and $\hat{b}_a$, calculated using

$$\alpha = \cos^{-1}(\hat{b}_m \cdot \hat{b}_a) \quad (6)$$

2.C.2. Tip localization accuracy

Let $t_m[t_{m,x}, t_{m,y}, t_{m,z}]$ and $t_a[t_{a,x}, t_{a,y}, t_{a,z}]$ be the needle tip positions of the manual and algorithm-based segmentations, respectively. Needle tip errors were defined as the 3D Euclidean distance $|\vec{d}_{tip}|$, where $\vec{d}_{tip} = t_a - t_m$. The x and y components of $\vec{d}_{tip}$ were also rotated to be expressed in terms of r and t components at point t_m. Principal component analysis was used to determine the primary directions of tip error variance and 95% prediction interval ellipsoids.[36,37]

2.C.3. Impact of image artifacts on segmentation accuracy

The medical physicist performing the manual segmentations subjectively classified each needle tip as obstructed, partially obstructed, or unobstructed by shadow artifacts based on needle tip appearance. Unobstructed needles had a high needle tip-to-background contrast, and did not appear to enter any signal voids. Obstructed needles had low needle tip-to-background contrast in the vicinity of obvious signal voids. Partially obstructed needles did not fit clearly into the other two categories, and typically had low tip-to-background contrast but did not enter any obvious signal voids. 3D tip errors of the automatic segmentations were stratified based on needle tip appearance, and median values were compared between groups. Statistical tests were performed in SPSS 23 (IBM, Armonk NY, USA).

3. RESULTS

Between 14 and 20 needles were inserted in each of the 12 patients for a total of 194. One hundred and ninety one of these needles were plastic FlexiGuide needles (Eckert & Ziegler Group, Berlin, DE) with 2.00 mm diameter, and three were metal interstitial needles with 1.65 mm diameter. All 194 needles were used as input in the segmentation algorithm, but four needles were excluded from geometric analysis including the three nonplastic needles, and one needle that extended beyond the edge of the SR3D image due to incorrect probe placement prior to image acquisition. All 194 needle tips were detectable intraoperatively using 2D ultrasound imaging incorporated in the clinical SAAR procedure, so were included in the treatment plans. Execution times of the algorithm are listed in Table I. The mean execution time was 11.0 s per patient, or 0.7 s per needle. Figure 5 shows example segmentations produced for two patients, indicating the 3D needle tip distances between manual and automatic segmentations. Treatment planning studies recommend needle tip localization accuracy within 3 mm^2 and previous HDR-BT imaging studies described tip errors in terms of 3 mm and 5 mm thresholds.[12,14] The geometric performance of the algorithm is summarized in terms of these thresholds in Table II.

3.A. Trajectory localization accuracy

Figure 6(a) displays a histogram of the angular trajectory errors of the automatic segmentations. About 83% of the 190 needle trajectories were identified by the algorithm within 3° of the corresponding manual segmentation. Figure 6(b) displays a histogram of 2D axial trajectory errors of the

TABLE I. Algorithm execution times.

Algorithm component	Mean (Stan. Dev.) execution time per patient (s)
Image filtering	3.44 (0.08)
Image binarization	1.13 (0.07)
Trajectory identification	3.23 (0.14)
Trajectory refinement	0.013 (0.001)
Needle tip localization	3.23 (0.28)
Manual trajectory labeling[a]	0.003 (0.001)
Total	11.04 (0.22)

[a]only includes computational time required to label candidate trajectories using manually identified points; does not include user-interaction time required to identify points.

TABLE II. Algorithm performance for 190 needles.

Error metric	% (#) of Needles
2D Axial trajectory error ≤3 mm	91 (173)
Trajectory angular error ≤3°	83 (157)
2D Axial tip error ≤3 mm	91 (172)
3D Tip error ≤3 mm	82 (155)
3D Tip error ≤5 mm	85 (161)
Reported failed segmentations[a]	6 (12)

[a]reported when no candidate needle trajectory is identified within 5 mm of the manually selected label point.

automatic segmentations. Ninety one percentage of needle trajectories were segmented within 3 mm error. Figure 6(c) displays a 2D plot of r and t trajectory error components along with the 95% prediction interval ellipse. The mean [95% prediction intervals] of the distribution in (t, r) were 0.28 [−1.74, 2.30] mm and −0.08 [−0.89, 0.73] mm, respectively. Two image artifacts incorrectly identified as needles had 2D trajectory errors >5 mm and were excluded from all 95% prediction interval calculations.

3.B. Tip localization accuracy

Figure 7(a) displays a histogram of 3D tip errors for the automatic segmentations. Eighty two percentage of needle tips were segmented within 3 mm error and 85% were segmented within 5 mm error. Figure 7(b) displays a 3D plot of t, r, and z tip error components along with the 95% prediction interval ellipsoid. The mean [95% prediction intervals] of the distribution in (t, r, z) were 0.05 [−1.58, 1.67] mm, −0.07 [−0.65, 0.51] mm, and 0.35 [−6.23, 6.93] mm, respectively. Figure 7(c) displays a highlighted view of the 2D tip error components in the r and t directions. Ninety one percentage of needle tips were identified with 2D errors in the axial plane within 3 mm.

3.C. Impact of image artifacts on segmentation accuracy

Of the 178 automatically segmented needles, 143 (80%) needles were classified as unobstructed, 20 (11%) as partially obstructed, and 15 (8%) as obstructed. Of the 12 needles reported as automatic segmentation failures, 1 (8%) was classified as unobstructed, 3 (25%) as partially obstructed, and 3 (25%) as obstructed. The remaining 5 (42%) were completely obstructed so could not be identified manually. Figure 8 displays histograms of 3D tip errors stratified by tip appearance for the automatic segmentations. Shapiro–Wilk tests indicated that the 3D tip errors were not normally distributed, with $P < 0.001$ for all groups. Medians (interquartile ranges) of the unobstructed, partially obstructed, and obstructed groups were 0.87 (1.03) mm, 1.49 (2.87) mm, and 1.54 (4.68) mm, respectively. A nonparametric independent-samples Kruskal–Wallis test indicated a significant effect of tip appearance on median 3D tip error ($P = 0.013$), and post hoc Mann–Whitney U tests indicated a significant pairwise difference between the unobstructed and partially obstructed groups ($P = 0.013$) but not between the unobstructed and obstructed groups ($P = 0.068$), or obstructed and partially obstructed groups ($P = 0.77$). The percentage of needles segmented within 3 mm error in the unobstructed, partially obstructed, and obstructed groups was 92%, 65%, and 67%, respectively.

4. DISCUSSION

We have presented an algorithm designed to segment multiple needles present in a 3D ultrasound image simultaneously without requiring the user to crop regions of interest containing one needle each. The segmentation algorithm identified 82% and 85% of needle tips with 3D tip error

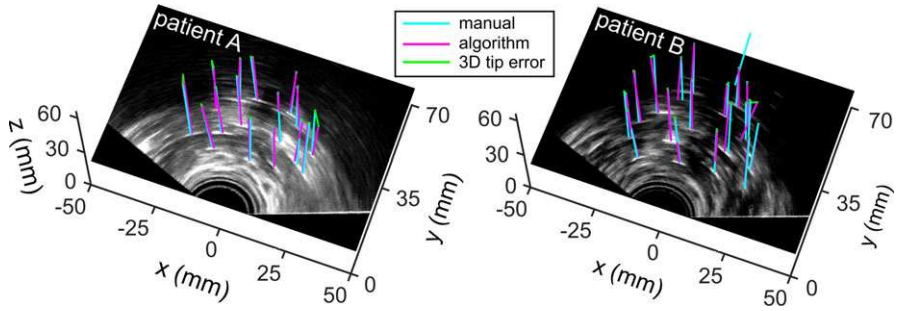

FIG. 5. Example segmentations from two patients intersecting an axial slice of the SR3D image. The algorithm did not identify a trajectory for the most anterior needle from patient B indicated by the absence of a 3D tip error vector. [Color figure can be viewed at wileyonlinelibrary.com]

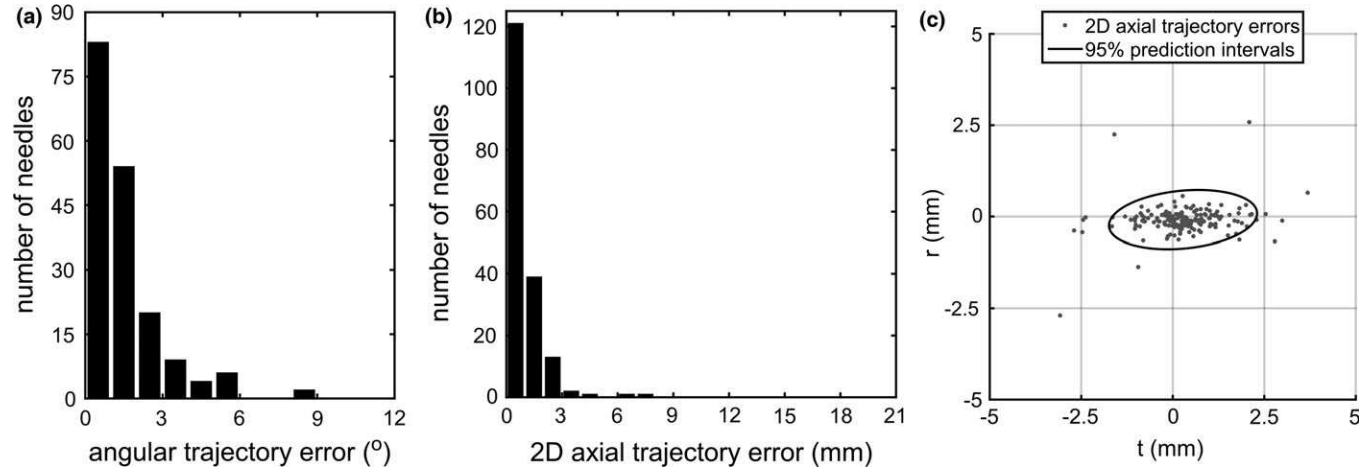

FIG. 6. (a-b) Histograms of angular trajectory error and 2D axial trajectory error of automatically segmented needles relative to the corresponding manual segmentations. (c) Plot of 2D axial trajectory error components expressed in terms of radial (r) and tangential (t) directions along with 95% prediction intervals. Two artifacts incorrectly identified as needles resulted in 2D axial trajectory errors >5 mm, so were occluded from (c) and excluded from the 95% prediction interval calculation.

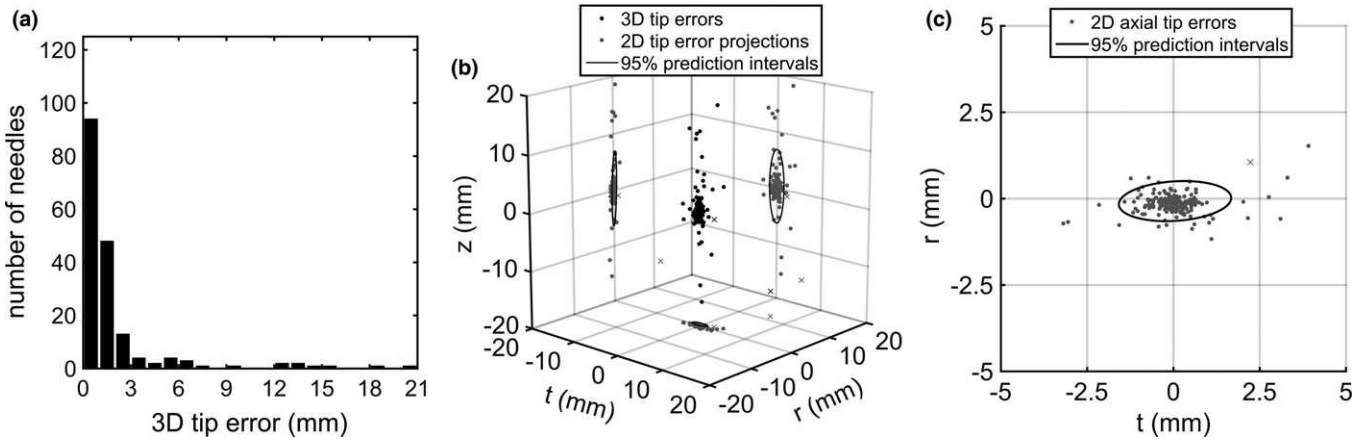

FIG. 7. (a) Histogram of 3D needle tip errors of automatically segmented needles relative to the corresponding manual segmentations. (b) Plot of 3D needle tip error components expressed in terms of radial (r), tangential (t), and superior/inferior (z) directions along with 2D error projections and 95% prediction interval ellipsoid projections. (c) Highlight of 2D axial needle tip error components along with 95% prediction interval ellipse. Two artifacts incorrectly identified as needles resulted in 2D axial trajectory errors >5 mm, so are indicated by x-marks and were excluded from the 95% prediction interval calculations in (b) and (c).

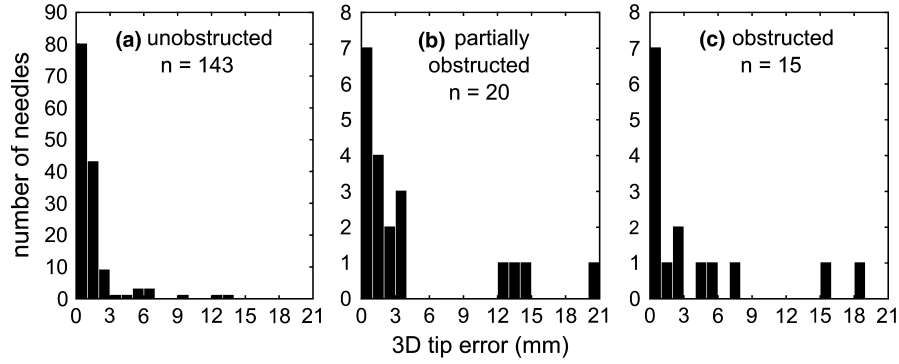

FIG. 8. Histograms of 3D tip errors stratified by needle tip appearance manually classified by a medical physicist. The number of needles included in each histogram (n) is indicated.

≤3 mm and ≤5 mm, respectively, and results may be considered in the context of manual tip localization, which was found to lead to 1D insertion depth errors ≤3 mm and ≤5 mm in 83% and 92% of needles, respectively, when compared to needle end-length measurements.[14] The average algorithm execution time of 11.0 s per patient is sufficient for

implementation in clinical HDR-BT workflows which typically take 1.5–3 h.

The 95% prediction intervals for the 3D tip errors were significantly larger in the z direction than the r or t directions, corresponding to the primary direction of needle insertion. This result suggests that tip localization remains a weakness of the algorithm. The z direction is also the primary error component for manual needle segmentation,[14] suggesting that image quality may also limit current tip localization performance. The 95% prediction intervals for both the 2D axial tip errors and 2D axial trajectory errors were also larger in the t direction than the r direction. This result corresponds to the differences in spatial resolution in these two directions, which are limited by the axial and elevational spatial resolutions of the sagittal transducer, and suggests that segmentation performance could be improved in the t direction by improving the transducer's elevational resolution.

A limitation of the current algorithm is the potential for large segmentation errors in the presence of nearby hyperechoic features and image artifacts such as reflections and shadows. For instance, three needles considered "unobstructed" had 3D tip errors >9 mm as shown in Figure 8(a). Examination of these cases revealed that incorrect tip positions were identified due to calcifications superior to the tip in two cases, and the presence of a reflection artifact near the tip in one case. These segmentations errors indicate the need for manual quality assurance, which would add time intraoperatively. However, it would be possible to automatically display image cross-sections containing each needle trajectory using the algorithm results to expedite the manual quality assurance procedure.

The algorithm failed to identify 12 needles, representing an overall false-negative rate of 6.3% of the 190 needles analyzed. Five of these needles (2.6%) also could not be detected manually due to the presence of shadow artifacts. The algorithm also incorrectly identified two image artifacts as needles representing a false-positive rate of 1.0%. Altogether, the segmentation failure rate is 7.3%. Previous studies investigating automatic needle segmentation only evaluated single needles. One study employed filtered intensity-based feature point classification and trajectory localization using the 3DHT, and reported segmentation failures for 30% of *in vivo* images containing single needles.[24] More recently, studies investigating phase grouping-based segmentation have reported failure rates as low as 4% for *in vivo* images containing single needles with optimized gain settings.[25] In the future, improvements in SR3D image quality will likely be required to mitigate the potential for manual and automatic segmentation failures as observed for 2.6% and 7.3% of needles, respectively, in this study. The ability to segment all needles using 2D ultrasound during the clinical SAAR procedure suggests that incorporating these dynamic 2D images into the segmentation workflow may provide improvements in robustness. Previous investigators have proposed the use of 2D ultrasound for automatic segmentation of HDR-BT needles, but did not report results for images containing multiple needles.[32] Based on observed limitations in SR3D image quality, a useful comparator of automatic segmentation variability would also be interobserver variability, and manual segmentations averaged among observers would represent a superior gold standard to the segmentations from a single observer used in this study.

Another limitation of the algorithm is the set of physical constraints on the shape, orientation, and distribution of needles that can be segmented. In terms of shape, the current algorithm only models straight needles. Brachytherapy needles can deflect when inserted in tissue,[33] and extensions of this algorithm may be required to model curvilinear needles to improve robustness. In terms of needle orientation, trajectories were limited to $\leq 10°$ from the axis of probe rotation (z-axis). This constraint reflected the needle trajectories we observed across patients, but may be violated when using an insertion template that allows larger insertion angles. In terms of needle distribution, a minimum 3 mm distance in the axial plane was enforced between adjacent needles, which also may be violated depending on the insertion template used. Finally, the tip localization procedure constrained insertion depths to the range [−12 mm, 10 mm] relative to the median insertion depth for that patient. Insertion depths may vary significantly depending on practice; for instance, needles may be inserted into the seminal vesicles and extend superiorly beyond the prostate base. In these instances, insertion depth limits may need to be relaxed, creating the potential for larger insertion depth errors than observed in this study. It may be possible to accommodate a wider range of insertion depths using measurements of needle end-lengths protruding from the insertion template to calculate patient-specific insertion depth constraints. A calibration can also be performed to enable the direct calculation of insertion depths within the image using needle end-lengths, rather than relying solely on the SR3D image intensities.[14,38] These measurements would add to the algorithm execution time, but have been shown to provide tip localization uncertainty of 0.7 mm in tissue mimicking phantoms.[38]

This study did not explicitly investigate the sensitivity of algorithm execution time and segmentation performance to algorithm parameter values. Beyond selecting parameter limits based on observed ranges, no further parameter optimization was performed for this patient cohort, limiting potential parameter over-fitting. The thresholds used to initialize the local peak identification algorithms used to identify feature points in section 2.B.2, accumulator peaks in section 2.B.3, and needle tips in section 2.B.6 were chosen empirically based on observed parameter ranges. In our experience, the local peak identification algorithms demonstrated low sensitivity to the thresholds used for initialization, but in the future these specific threshold values should be validated using an independent image set.

5. CONCLUSIONS

We have presented an automatic needle segmentation algorithm for 3D ultrasound images containing multiple

needles for high-dose-rate prostate brachytherapy treatment planning, and demonstrated the algorithm's geometric performance with images from 12 patients containing 190 needles. Accurate needle localization is critical for HDR-BT treatment planning. Automatic segmentation approaches will not replace manual approaches until equivalence or superiority in geometric accuracy and robustness can be demonstrated. However, segmentation algorithms that add negligible time to the procedure may still be of significant use for either manual segmentation initialization or quality assurance. The speed and geometric accuracy of the presented algorithm indicate that it may provide improvements in clinical workflow efficiency for modern 3D ultrasound-guided high-dose-rate prostate brachytherapy.

ACKNOWLEDGMENTS

This study was supported by the Canadian Institutes of Health Research (CIHR, funding reference number 140352), the Cancer Research and Technology Transfer strategic training program (CaRTT), and the Ontario Institute for Cancer Research (OICR) Imaging Translation program.

CONFLICTS OF INTEREST

The authors have no relevant conflicts of interest to disclose.

APPENDIX

A. MANUAL SEGMENTATION ANALYSIS

Figure A1a shows a histogram of needle trajectory angles relative to the z-axis for all 185 plastic needles that could be manually segmented, demonstrating that the largest angle was <10°. The elevational angle (θ) search space of randomized 3DHT was then limited to the range [0°, 10°] as described in section 2.B.3. Figure A1(b) shows a histogram of the shortest distance in the axial plane to the nearest adjacent needle within the SR3D image for the manually segmented needles. Three pairs of needles had distances between one another <3 mm (2.9 mm, 2.7 mm, and 2.1 mm). Five of these needles were considered partially obstructed or obstructed by shadow artifacts at the time of manual segmentation, and the diameter of the plastic needles used in this study was 2 mm. A minimum separation distance of 3 mm in the axial plane was enforced between feature points as described in section 2.B.2. Figure A2(a) shows a boxplot of the length of each needle within the SR3D image, referred to as insertion depths, for each individual patient and all patients combined. Figure A2(b) then shows a boxplot of insertion depths after subtracting the median insertion depth for each patient. Limits of −12 mm and 10 mm are indicated, which encompass 98% of all needles. These limits were used to constrain the insertion depth search space in the second step of the tip localization algorithm, as described in section 2.B.6.

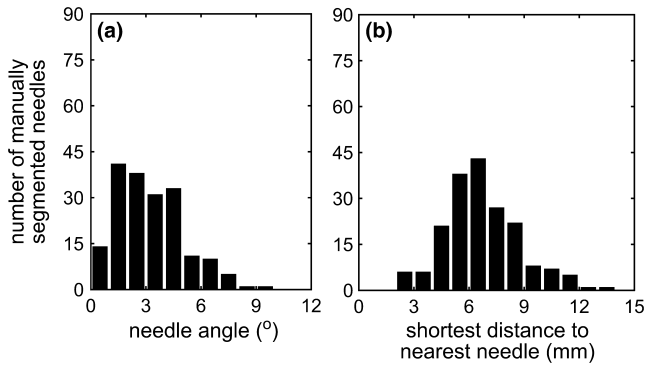

FIG. A1. (a) Histogram of needle trajectory angles relative to the superior/inferior (z)-axis and A1(b) histogram of the shortest distance in the axial plane to the nearest adjacent needle within the SR3D image for 185 manually segmented needles.

B. SIGNAL INTENSITY PROFILE ANALYSIS FOR TIP LOCALIZATION

B.1. Oriented subvolume cropping

Intensity profiles were obtained by cropping regions of interest surrounding each trajectory, then filtering and averaging the signal intensity in directions normal to the trajectory. The cropping region was 1.6 mm in the radial direction, and 4.7 mm in the tangential direction, corresponding to the intervals expected to contain 95% of the signal intensity distribution based on the standard deviations used by the filtering kernel. These cropping limits were applied by defining a local coordinate system (x', y', z'), with the z'-axis aligned along the needle trajectory, the x'-axis aligned along the tangential (t) image direction, and the y'-axis aligned along the radial (r) image direction at each point along the needle trajectory. Subvolume cropping was performed with $0.16 \times 0.16 \times 0.16$ mm^3 voxel dimensions.

B.2. Subvolume filtering

Following cropping, the cropped signal intensity values were filtered in the y' direction using the intensity-curvature-based filter as described in section 2.B.1, but to preserve spatial resolution in the insertion direction the signal intensity was not convolved with a uniform distribution in the z' direction. Following filtering, signal intensities were averaged in the x' and y' directions to produce 1D intensity profiles as a function of z' as shown in Fig. 4.

B.3. Signal intensity profile analysis

The needle tip corresponds to a signal intensity drop at the most superior point along the needle trajectory. Intensity "breaks" along a needle trajectory caused by imaging artifacts can cause intensity drops preceding the needle tip; however, the drop associated with the visible needle tip will be the most superior when inserted transperineally. Figure 4(a)–4(c)

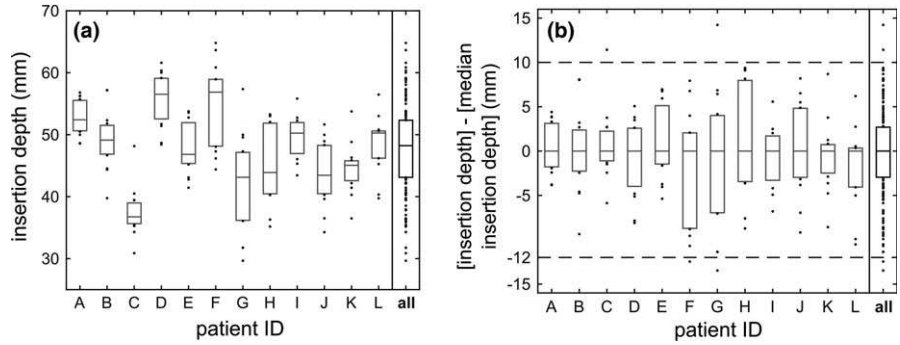

FIG. A2. (a) Boxplots of insertion depths (length of the needle within the SR3D image) of the 185 manually segmented needles for each individual patient, and all patients combined. (b) Boxplots of insertion depths after subtracting the median insertion depth for each patient. Horizontal lines at −12 mm and 10 mm indicate the insertion depth limits used by the tip localization algorithm. In all plots the center lines indicate median value, boxes indicate interquartile range, and points indicate values outside of the interquartile range.

displays cross-sections and intensity profiles of a needle with a signal intensity break inferior to the tip location. The first derivative of the 1D signal intensity profile was calculated by finding the intensity slope within 2.5 mm of each point using linear least-squares, as shown in Fig. 4(d). This derivative profile was normalized by the maximum value, and all local peaks with values greater than 0.7 were identified using MATLAB's *findpeaks* function, and the tip was selected as the most superior of these peaks.

C. RADIAL-TANGENTIAL ERROR COMPONENTS

Let $p_m\left[p_{m,x}, p_{m,y}\right]$ and $p_a\left[p_{a,x}, p_{a,y}\right]$ be the 2D axial coordinates of corresponding manual and algorithm-based segmentations. The 2D axial distance between these points is $\left|\vec{d}\right|$, where $\vec{d} = p_a - p_m$. To express $\vec{d}$ in terms of the r and t components at point p_m, a rotation matrix A was defined that effectively rotates the y-coordinate into $\vec{r}$ and the x-coordinate into $\vec{t}$ at point p_m, expressed as

$$A = \begin{pmatrix} \frac{1}{\sqrt{1+u^2}} & \frac{u}{\sqrt{1+u^2}} \\ \frac{-u}{\sqrt{1+u^2}} & \frac{1}{\sqrt{1+u^2}} \end{pmatrix} \tag{A1}$$

$$u = \frac{p_{m,x}}{p_{m,y}} \tag{A2}$$

This rotation matrix was applied to $\vec{d}$ to obtain the r and t components while preserving the length $\left|\vec{d}\right|$ in the rotated coordinate system. This method was used to find the r and t trajectory error components in section 2.C.1, and the r and t tip error components in section 2.C.2.

[a]Author to whom correspondence should be addressed. Electronic mail: whrinivi@uwo.ca; Telephone: (519) 661-2111 x80419.

REFERENCES

1. Siebert FA, Hirt M, Niehoff P, Kovács G. Imaging of implant needles for real-time HDR-brachytherapy prostate treatment using biplane ultrasound transducers. *Med Phys*. 2009;36:3406–3412.
2. Tiong A, Bydder S, Ebbert M, et al. A small tolerance for catheter displacement in high-dose rate prostate brachytherapy is necessary and feasible. *Int J Radiat Oncol Biol Phys*. 2010;76:1066–1072.
3. Mason J, Al-Qaisieh B, Bownes P, Thwaites D, Henry A. Dosimetry modeling for focal high-dose-rate prostate brachytherapy. *Brachytherapy*. 2014;13:611–617.
4. Hoskin PJ, Colombo A, Henry A, et al. GEC/ESTRO recommendations on high dose rate afterloading brachytherapy for localised prostate cancer: An update. *Radiother Oncol*. 2013;107:325–332.
5. Kolotas C, Baltas D, Zamboglou N. CT-based interstitial HDR brachytherapy. *Strahlentherapie und Onkol*. 1999;175:419–427.
6. Holly R, Morton GC, Sankreacha R, et al. Use of cone-beam imaging to correct for catheter displacement in high dose-rate prostate brachytherapy. *Brachytherapy*. 2011;10:299–305.
7. Ares C, Popowski Y, Pampallona S, et al. Hypofractionated boost with high-dose-rate brachytherapy and open magnetic resonance imaging-guided implants for locally aggressive prostate cancer: A Sequential Dose-Escalation Pilot Study. *Int J Radiat Oncol Biol Phys*. 2009;75:656–663.
8. Schick U, Popowski Y, Nouet P, et al. High-dose-rate brachytherapy boost to the dominant intra-prostatic tumor region: Hemi-irradiation of prostate cancer. *Prostate*. 2011;71:1309–1316.
9. Ménard C, Susil RC, Choyke P, et al. MRI-guided HDR prostate brachytherapy in standard 1.5T scanner. *Int J Radiat Oncol Biol Phys*. 2004;59:1414–1423.
10. Murgic J, Chung P, Berlin A, et al. Lessons learned using an MRI-only workflow during high-dose-rate brachytherapy for prostate cancer. *Brachytherapy*. 2015;15:147–155.
11. Schmid M, Crook J, Batchelar D, et al. A phantom study to assess accuracy of needle identification in real-time planning of ultrasound-guided high-dose-rate prostate implants. *Brachytherapy*. 2013;12:56–64.
12. Batchelar D, Gaztañaga M, Schmid M, Araujo C, Bachand F, Crook J. Validation study of ultrasound-based high-dose-rate prostate brachytherapy planning compared with CT-based planning. *Brachytherapy*. 2014;13:75–79.
13. Morton GC. Prostate high-dose-rate brachytherapy: Transrectal ultrasound based planning, a technical note. *Pract Radiat Oncol*. 2015;5:238–240.
14. Hrinivich WT, Hoover DA, Surry K, et al. Three-dimensional transrectal ultrasound guided high-dose-rate prostate brachytherapy: A comparison of needle segmentation accuracy with two-dimensional image guidance. *Brachytherapy*. 2016;15:231–239.
15. Fenster A, Downey DB. Three-Dimensional Ultrasound Imaging. *Annu Rev Biomed Eng*. 2000;2:457–475.
16. Bax J, Smith D, Bartha L, et al. A compact mechatronic system for 3D ultrasound guided prostate interventions. *Med Phys*. 2011;38:1055–1069.
17. Ding M, Cardinal HN, Fenster A. Automatic needle segmentation in three-dimensional ultrasound images using two orthogonal two-dimensional image projections. *Med Phys*. 2003;30:222–234.

18. Aboofazeli M, Abolmaesumi P, Mousavi P, Fichtinger G. A new scheme for curved needle segmentation in three-dimensional ultrasound images. In Proc. IEEE Int. Symp. Biomed. Imaging 2009, pp. 1067–1070.
19. Barva M, Uherčík M, Mari J. Parallel integral projection transform for straight electrode localization in 3-D ultrasound images. *IEEE Trans Ferroelect Freq Control*. 2008;55:1559–1569.
20. Zhou H, Qiu W, Ding M, Zhang S. Automatic needle segmentation in 3D ultrasound images using 3D improved Hough transform. In Proc. SPIE Med. Imag.: Image-Guided Procedures Modeling 2008, pp. 691821-1–691821-9.
21. Qiu W, Ding M, Yuchi M. Needle segmentation using 3D quick randomized hough transform. In 1st Int. Conf. Intell. Networks Intell. Syst. ICINIS 2008, pp. 449–452.
22. Zhao S, Qiu W, Ming Y, Ding M. Needle segmentation in 3D ultrasound images based on phase grouping. In Proc. SPIE Med. Imag.: Image-Guided Procedures Modeling 2009, pp. 74971L–74971L-10.
23. Qiu W, Ding M, Yuchi M. Electrode Localization in 3D Ultrasound Images Using 3D Phase Grouping and Randomized Hough Transform. In Electrode Localization 3D Ultrasound Images Using 3D Phase Group. Randomized Hough Transform(IEEE), 2010, pp. 202–205.
24. Qiu W, Yuchi M, Ding M, Tessier D, Fenster A. Needle segmentation using 3D Hough transform in 3D TRUS guided prostate transperineal therapy. *Med Phys*. 2013;40:42902.
25. Qiu W, Yuchi M, Ding M. Phase grouping-based needle segmentation in 3-D trans-rectal ultrasound-guided prostate trans-perineal therapy. *Ultrasound Med Biol*. 2014;40:804–816.
26. Beigi P, Rohling R, Salcudean T, Lessoway VA, Ng GC. Needle trajectory and tip localization in real-time 3-D ultrasound using a moving stylus. *Ultrasound Med Biol*. 2015;41:2057–2070.
27. Luengo Hendriks CL, Van Ginkel M, Verbeek PW, Van Vliet LJ. The generalized Radon transform: Sampling, accuracy and memory considerations. *Pattern Recognit*. 2005;38:2494–2505.
28. Novotny PM, Stoll JA, Vasilyev V, et al. GPU based real-time instrument tracking with three-dimensional ultrasound. *Med Image Anal*. 2007;11:458–464.
29. Neshat HRS, Patel RV. Real-time parametric curved needle segmentation in 3D ultrasound images. In 2nd IEEE RAS EMBS Int. Conf. Biomed. Robot. Biomechatronics 2008, pp. 670–675.
30. Uherčík M, Kybic J, Liebgott H, Cachard C. Model fitting using ransac for surgical tool localization in 3-D ultrasound images. *IEEE Trans Biomed Eng*. 2010;57:1907–1916.
31. Uherčík M, Kybic J, Zhao Y, Cachard C, Liebgott H. Line filtering for surgical tool localization in 3D ultrasound images. *Comput Biol Med*. 2013;43:2036–2045.
32. Buzurovic I, Misic V, Yu Y. Needle identification in high-dose-rate prostate brachytherapy using ultrasound imaging modality. In Proc. Annu. Int. Conf. IEEE Eng. Med. Biol. Soc. EMBS 2012, pp. 476–479.
33. Wan G, Wei Z, Gardi L, Downey DB, Fenster A. Brachytherapy needle deflection evaluation and correction. *Med Phys*. 2005;32:902–909.
34. Perona P, Malik J. Scale-space and edge detection using anisotropic diffusion. *IEEE Trans Pattern Anal Mach Intell*. 1990;12:629–639.
35. Peikari M, Chen TK, Lasso A, Heffter T, Fichtinger G, Burdette EC. Characterization of ultrasound elevation beamwidth artifacts for prostate brachytherapy needle insertion. *Med Phys*. 2012;39:246–256.
36. Irwin MR, Downey DB, Gardi L, Fenster A. Registered 3-D ultrasound and digital stereotactic mammography for breast biopsy guidance. *IEEE Trans Med Imaging*. 2008;27:391–401.
37. Karnik VV, Fenster A, Bax J, Romagnoli C, Ward AD. Evaluation of intersession 3D-TRUS to 3D-TRUS image registration for repeat prostate biopsies. *Med Phys*. 2011;38:1832–1843.
38. Zheng D, Todor DA. A novel method for accurate needle-tip identification in trans-rectal ultrasound-based high-dose-rate prostate brachytherapy. *Brachytherapy*. 2011;10:466–473.

Mobius3D

THE COMPLETE PATIENT QA SYSTEM

3D PATIENT PLAN QA

3D IMRT/VMAT PRE TREATMENT QA

3D *IN VIVO* DAILY TREATMENT QA

ONLINE PATIENT POSITIONING QA

Upgrade your patient safety by bridging the gap between patient QA and machine QA:

DoseLab, the complete TG-142 solution, is now integrated into Mobius3D!

Visit mobiusmed.com/mobius3d to learn more or register for a bi-weekly webinar at mobiusmed.com/webinars

MOBIUS MEDICAL SYSTEMS
INNOVATIVE SOFTWARE FOR MODERN RADIATION ONCOLOGY

Toward a 3D transrectal ultrasound system for verification of needle placement during high-dose-rate interstitial gynecologic brachytherapy

Jessica Robin Rodgers[a)]
Biomedical Engineering Graduate Program, The University of Western Ontario, London, ON N6A 3K7, Canada
Robarts Research Institute, The University of Western Ontario, London, ON N6A 5B7, Canada

Kathleen Surry
Department of Medical Physics, London Regional Cancer Program, London, ON N6A 5W9, Canada

Eric Leung
Department of Radiation Oncology, Odette Cancer Centre, Sunnybrook Health Sciences Centre, Toronto, ON M4N 3M5, Canada

David D'Souza
Department of Radiation Oncology, London Regional Cancer Program, London, ON N6A 5W9, Canada

Aaron Fenster
Biomedical Engineering Graduate Program, The University of Western Ontario, London, ON N6A 3K7, Canada
Robarts Research Institute, The University of Western Ontario, London, ON N6A 5B7, Canada

(Received 5 October 2016; revised 13 January 2017; accepted for publication 9 March 2017; published xx xxxx xxxx)

Purpose: Treatment for gynecologic cancers, such as cervical, recurrent endometrial, and vaginal malignancies, commonly includes external-beam radiation and brachytherapy. In high-dose-rate (HDR) interstitial gynecologic brachytherapy, radiation treatment is delivered via hollow needles that are typically inserted through a template on the perineum with a cylinder placed in the vagina for stability. Despite the need for precise needle placement to minimize complications and provide optimal treatment, there is no standard intra-operative image-guidance for this procedure. While some image-guidance techniques have been proposed, including magnetic resonance (MR) imaging, X-ray computed tomography (CT), and two-dimensional (2D) transrectal ultrasound (TRUS), these techniques have not been widely adopted. In order to provide intra-operative needle visualization and localization during interstitial brachytherapy, we have developed a three-dimensional (3D) TRUS system. This study describes the 3D TRUS system and reports on the system validation and results from a proof-of-concept patient study.

Methods: To obtain a 3D TRUS image, the system rotates a conventional 2D endocavity transducer through 170 degrees in 12 s, reconstructing the 2D frames into a 3D image in real-time. The geometry of the reconstruction was validated using two geometric phantoms to ensure the accuracy of the linear measurements in each of the image coordinate directions and the volumetric accuracy of the system. An agar phantom including vaginal and rectal canals, as well as a model uterus and tumor, was designed and used to test the visualization and localization of the interstitial needles under idealized conditions by comparing the needles' positions between the 3D TRUS scan and a registered MR image. Five patients undergoing HDR interstitial gynecologic brachytherapy were imaged using the 3D TRUS system following the insertion of all needles. This image was manually, rigidly registered to the clinical postinsertion CT scan based on the vaginal cylinder of the needle template. The positions of the tips and the trajectory of the needle paths were compared between the modalities.

Results: The observed geometric errors of the system were ≤ 0.3 mm in each of the three coordinate planes of the 3D US image and the mean measured volumetric error was 0.10 cm^3. In the phantom study, the mean needle tip difference was 1.54 ± 0.71 mm and the mean trajectory difference was 0.94 ± 0.89 degrees ($n = 14$). In the *in vivo* study, a total of 73 needles were placed, of which 88% of needles were visible and 79% of tips were identifiable in the 3D TRUS images. Six of the nine needles that were not visible were due to shadowing artifacts created by the presence of the vaginal cylinder of the needle template. The mean distance between corresponding needle tips in the two modalities was 3.82 ± 1.86 mm and the mean trajectory difference was 3.04 ± 1.63 degrees for the five patients.

Conclusions: In this proof-of-concept study, the 3D TRUS system allowed for localization of needles not obscured by shadowing artifacts, providing a method for visualizing needles intra-operatively during HDR interstitial brachytherapy of gynecologic cancers and providing the potential for 3D image-guidance. [https://doi.org/10.1002/mp.12221]

Key words: 3D ultrasound, gynecologic brachytherapy, interstitial brachytherapy, transrectal ultrasound

1. INTRODUCTION

Gynecologic malignancies, including cervical, recurrent endometrial, and vaginal cancers, are the fourth leading cause of female cancer mortality worldwide.[1] These cancers are commonly treated with external-beam radiation and brachytherapy as part of standard-of-care treatment, in order to increase the radiation dose delivered to the tumor in comparison to the surrounding normal tissues.[2,3] A perineal interstitial approach to gynecologic brachytherapy may be indicated for cervical cancers or vaginal tumors, including primary vaginal tumors or recurrent cancers in the vagina.[3,4]

In high-dose-rate (HDR) interstitial brachytherapy, hollow needles are inserted directly into the tumor and surrounding tissues and a single high-activity radiation source is temporarily placed at planned positions via these needles.[3] During the needle insertion procedure for HDR interstitial gynecologic brachytherapy, the patient is placed under general or spinal anesthesia and the patients' legs are placed in the lithotomy position.[3] A clinical examination is then performed and a Foley catheter is placed into the patient's bladder.[3] For interstitial gynecologic brachytherapy, needles are often inserted through a template on the perineum, which includes a central cylinder that is placed into the vagina to separate the vaginal walls and provide stability.[5] In cases where cervical cancer with an intact uterus is being treated with a perineal interstitial brachytherapy approach, an additional tandem is placed through the center of the cylinder; however, all patients in this study were diagnosed with vaginal tumors and thus, the tandem was not included in the procedure. Due to the diverse clinical scenarios treated using interstitial brachytherapy, the distribution, placement depth, and number of needles placed, and thereby the duration of the procedure differs greatly. At our institution, an average of 12 needles are typically placed[6] and the duration of the insertion procedure is usually about an hour, including induction of anesthesia, examination, insertion, and recovery. Needle insertion is followed by imaging to confirm needle positions and create a dose plan; most institutions acquire these postinsertion images using X-ray computed tomography (CT), though magnetic resonance (MR) imaging is used at some institutions. Typically, an Iridium-192 HDR radiation source is used for treatment with a 5 mm step size between source dwell positions and the dose is delivered in two to four fractions with a minimum of six hours in between.[6] The standard dose prescribed to the gross disease is typically 70–90 Gy for vaginal cancers and 60 Gy delivered to the vaginal surface,[3] with 19.5 Gy typically delivered via HDR brachytherapy in three fractions at our institution. Following the treatment, the template, vaginal cylinder, and all needles are removed.

Precise placement of needles is critical during the procedure in order to optimize local control while minimizing major side effects, especially by avoiding nearby organs at risk (OAR), including the bladder and rectum;[2] however, this is assessed after the procedure as there is currently no standard intra-operative image-guidance techniques for the adaptive placement of needles during HDR interstitial gynecologic brachytherapy. This creates a substantial reliance on the experience of the radiation oncologist and on preoperative images. Precise needle placement to avoid the OAR is particularly important as stainless steel or titanium needles with a 0.5 mm solid tip are often used for this procedure and therefore the needle tips extend beyond the target region to ensure dose coverage, potentially impinging on the OAR positions. The lack of image-guidance during this procedure can lead to inaccurate needle placement, resulting in suboptimal treatment.[7,8]

Various methods of needle guidance during interstitial gynecologic brachytherapy have been proposed, including fluoroscopy,[9] laparotomy or laparoscopy,[10–12] ultrasound (US),[13–17] CT,[18] and MR guidance.[19–22] Fluoroscopy is limited as soft tissue definition is poor and needle misalignments cannot be visualized in both the coronal and sagittal planes in a single image acquisition, therefore requiring alternating between these directions to get a comprehensive view of needle placement.[9,23] Open laparotomy is limited in its use as it is a major surgical procedure, increasing risk of complications and typically requiring a longer postoperative hospital stay.[13] In addition to being more invasive procedures than the other proposed imaging modalities, one of the main limitations of both laparotomy and laparoscopy is that needle placement must be determined by visualization from above and therefore does not usually allow for visualization of parts of the bladder, uterus, cervix, and vagina.[13] This is particularly an issue for vaginal tumors and upper vaginal disease, as well as tumors in close proximity to the OAR, as a needle may not be visualized passing through the bladder or rectum.[13] Two-dimensional (2D) transabdominal US is often used to visualize the most anterior needles and prevent penetration of the bladder,[16] and 2D transrectal ultrasound (TRUS) has been investigated as it allows for imaging in closer proximity to the region-of-interest.[13–15] In particular, Stock et al.[13] recommended the use of side-fire TRUS in order to visualize the depth and placement of needles. As conventional TRUS transducers provide a 2D planar image, the needles are sometimes localized using the transverse plane of a biplane probe first and then switching to the longitudinal, side-fire element to assess needle depth.[13] This demonstrates one of the main limitations of 2D US imaging, as the clinician must mentally collate the 2D image planes to form a three-dimensional (3D) impression of the needle position and relevant structures, such as the OAR, which is inefficient and time-consuming.[24,25] Additionally, it is difficult to find the same 2D US plane placement and orientation at a later time, limiting its use for planning and monitoring therapy, and the patient's position and anatomical restrictions may prevent the optimal placement of the 2D image plane.[24,25] Therefore, although 2D US imaging can provide real-time visualization of needles, the use of 2D images is prone to variability and inaccuracy when localizing needles and is highly operator-dependent.

Three-dimensional image-guidance can mitigate many of the issues associated with 2D imaging, as the user is provided with a 3D image rather than mentally integrating the 2D

image planes and can manipulate the image to view any cross-section without restriction,[24] allowing for improved visualization of needle depth and trajectory, as well as avoidance of the OAR.[3] 3D imaging is particularly beneficial in complex cases, including tumors near the rectum, and may contribute to potentially fewer side effects.[3] Intra-operative 3D imaging also enables misdirected needles to be repositioned immediately, whereas misplaced needles may not be usable for treatment if discovered during postinsertion imaging, and intra-operative 3D visualization may allow for fewer needles to be inserted.[2,3] Lee et al.[18] proposed performing needle insertion under CT guidance, using an iterative approach of inserting needles followed by verification of needle positions. Kapur et al.[20] reported a similar approach under 3T MR guidance and Viswanathan et al.[22] proposed real-time 3D image-guidance using a specialized interventional 0.5T MR system. While these guidance techniques provide the benefits of 3D imaging, they are limited by increased anesthesia and treatment times and require specialized equipment and procedure suites, restricting accessibility to a few instiutions.[3]

We have developed a 3D TRUS system in order to provide intra-operative needle visualization during HDR interstitial gynecologic brachytherapy. This system was modified from a 3D TRUS system previously designed in our laboratory for prostate imaging[26] and the preliminary results of the use of this system for gynecologic brachytherapy have been presented in Rodgers et al.[17] The objective of this study was to determine if this system will allow for intra-operative needle visualization and localization, providing the advantages of 3D image-guidance over the previously described 2D US approaches. In this paper, we describe the 3D TRUS system and report on the system validation using phantoms and results from a proof-of-concept patient study comparing needle positions in 3D TRUS images to CT images for five patients.

2. MATERIALS AND METHODS

2.A. 3D TRUS system

We developed a 3D TRUS system that is compatible with conventional 2D TRUS side-fire transducers.[17] In this study, a BK Falcon 2101 EXL US system with an 8658 endocavity biplane US probe (BK Medical, Boston, MA, USA) was used to acquire phantom images and a BK Profocus 2202 diagnostic US system with an 8848 endocavity biplane US probe (BK Medical, Boston, MA, USA) was used to acquire patient images. To obtain a 3D US image, the clinical 2D transducer is secured in a cradle, which is rotated on its central axis through 170 degrees by a motorized mover, following the tilt scanning approach described in Fenster et al.[24] The rotational mover is powered by a Faulhaber 2224u012SR DC motor with an IE2-256 encoder (MicroMo Electronics, Clearwater, FL, USA) inside a motor housing and connected to a MCDC 3006S controller (MicroMo Electronics, Clearwater, FL, USA), which is linked to a desktop computer through a USB connection. The 3D US scanner is shown in Fig. 1. During operation, the 3D US scanner is positioned at the center of the region-of-interest and held securely by the user around the motor housing. The cradle is first rotated to one angular extreme and an Epiphan VGA2USB video frame grabber (Epiphan Systems Inc., Ottawa, ON, Canada) transmits 300 2D US images from the clinical US machine's video output to the desktop computer as the scan is performed. The scan is controlled by reconstruction and visualization software developed in our laboratory,[24–29] which uses the 300 2D US images (at angular intervals of 0.57 degrees) and motor information to reconstruct the 2D frames into a 3D US image ($488 \times 500 \times 1010$ voxels with voxel size of $0.144 \times 0.145 \times 0.145$ mm^3) in real-time as the frames are collected during the 12 s scan time.

2.B. Geometric phantom validation

The linear measurements in each of the Cartesian image coordinate directions were validated using a phantom composed of four layers, each made up of a 10 mm square grid, in order to verify that the geometry of the reconstructed 3D US images is correctly calibrated. The layers were offset to prevent shadowing with resulting diagonal distances of 10.3 mm and 12.5 mm between corresponding strings in adjacent layers. This phantom was placed in a solution of distilled water and 7% glycerol (Sigma Aldrich, Co., St. Louis, MO, USA) by mass, in which the speed of sound was approximately 1540 m/s.[30] The visualization software developed in our laboratory[24,25] was used to measure the distances between the strings in each of the coordinate planes of the images.

In order to further validate the geometric reconstruction, an agar phantom, shown in Fig. 2(a), was used to verify the volumetric accuracy of the 3D US image. The phantom background was an agar mixture containing 35 g agar powder (Sigma Aldrich, Co., St. Louis, MO, USA), 80 mL glycerol (Sigma Aldrich, Co., St. Louis, MO, USA) and 10 g Sigma-Cell cellulose powder (Sigma Aldrich, Co., St. Louis, MO, USA) per 1 L distilled water to mimic soft tissue scatter in US images.[30] A cervical tumor was segmented from a patient MR image and used to 3D print a tumor mold with a volume of 46.57 cm^3. In order to create contrast between the tumor

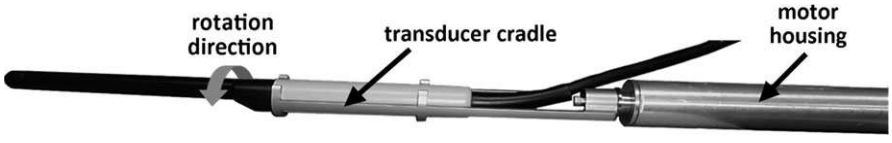

FIG. 1. 3D TRUS scanner with key features indicated.

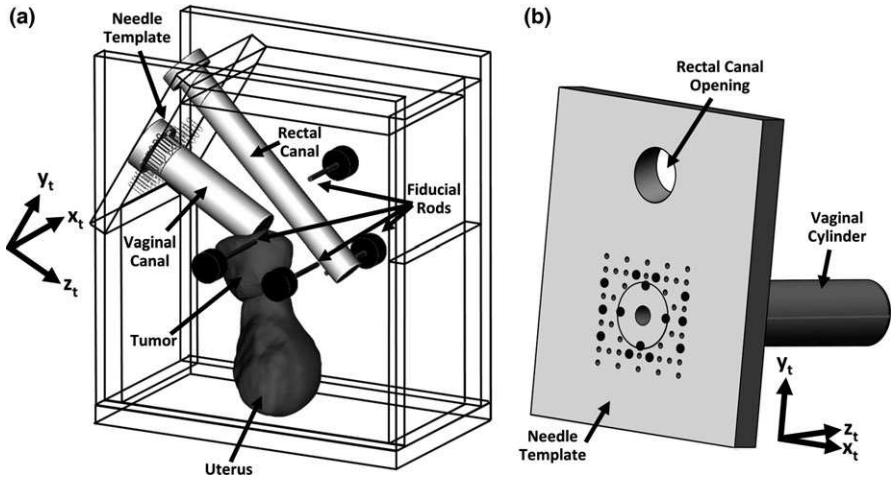

FIG. 2. (a) Pelvic phantom box showing the positions of the model tumor and uterus, the four fiducial rods, the needle template, and the vaginal and rectal canals. (b) Needle template face of the phantom box with the template coordinate directions shown, including the vaginal cylinder in place and the 14 template holes used during the phantom study emphasized in black.

and background, the concentration of cellulose powder in the agar mixture used to fill the tumor mold was modified to 5.28 g cellulose powder per 1 L distilled water. This cellulose concentration for the tumor was chosen based on the relative intensity between tumor and background tissues typically seen in US images. A typical uterus was also segmented from a patient image and formed from the agar mixture to provide an additional landmark in the US images (6.72 g cellulose powder per 1 L distilled water). Tungsten powder (Sigma Chemical, St. Louis, MO, USA) was also added to both the tumor and uterus in differing concentrations (0.44% and 0.87% by mass, respectively) to generate contrast in a phantom that is compatible with both US and MR scans.[31,32] Both the tumor and uterus were embedded into the background agar and imaged using the 3D US scanner. Using our visualization software,[24,25] points were manually selected on the boundary of the tumor and a 3D mesh was fit through these points. The procedure was repeated three times and the resulting tumor volumes were calculated. The volumes of these segmentations were then used to further validate the reconstruction.

2.C. Pelvic phantom study

The volumetric phantom described above was designed to include a canal to accommodate the TRUS transducer, as well as a vaginal canal and needle template (including vaginal cylinder) approximating typical patient geometries, and included four fiducial marking rods as indicated in Fig. 2(a). The rectal and vaginal canals were placed at a 15 degree angle to one another, representing a typical patient geometry. Fourteen stainless steel needles were inserted in a common symmetric configuration, shown in Fig. 2(b), and imaged using the 3D TRUS system in order to test the visualization of the needles under idealized conditions. Following the 3D US scan, the needles were removed and the needle tracks filled with water using a small syringe to improve visualization in MR imaging, which was used as the geometric gold standard to compare against the 3D US images. The phantom was then scanned with a 3.0T Discovery MR750 scanner (General Electric Healthcare, Milwaukee, WI, USA) using a sagittal T2 weighted sequence (TR 2500 ms, TE 106.83 ms, echo train 100, scanning matrix 256 × 256, DFOV 30.0 × 30.0 cm, slice thickness 1.2 mm). Using our visualization software,[24,25] the 3D US and MR images were manually, rigidly registered[33] based on the template's vaginal cylinder and the four fiducial rods included in the phantom. For each image, the position of each needle tip and a second point along each needle path was selected. The needle trajectory difference and 3D Euclidean distance between the needle tips were calculated for each needle to compare the positions of the corresponding needles between the two modalities. Denoting the needle tip positions in Cartesian coordinates as $\boldsymbol{t_{us}} = (x_{us}, y_{us}, z_{us})$ and $\boldsymbol{t_{ct}} = (x_{ct}, y_{ct}, z_{ct})$ in 3D TRUS and CT, respectively, the 3D Euclidean distance,[34] $d(\boldsymbol{t_{us}}, \boldsymbol{t_{ct}})$, is calculated for each needle as

$$d(\boldsymbol{t_{us}}, \boldsymbol{t_{ct}}) = \sqrt{(x_{us} - x_{ct})^2 + (y_{us} - y_{ct})^2 + (z_{us} - z_{ct})^2}. \quad (1)$$

For each needle, the trajectory is a vector from the second point on the needle path directed toward the needle tip and is defined in 3D TRUS and CT as $\boldsymbol{n_{us}}$ and $\boldsymbol{n_{ct}}$, respectively. The angular difference,[34] Θ, between the trajectories is calculated as

$$\theta = \arccos \frac{\boldsymbol{n_{us}} \cdot \boldsymbol{n_{ct}}}{\|\boldsymbol{n_{us}}\| \|\boldsymbol{n_{ct}}\|}. \quad (2)$$

The relationship between the rectal and vaginal canals was used to transform the needle tip positions into coordinates relative to the needle template, denoted $(\boldsymbol{x_t}, \boldsymbol{y_t}, \boldsymbol{z_t})$, such that $\boldsymbol{x_t}$ represents the left/right direction on the template grid, $\boldsymbol{y_t}$ represents the down/up direction on the template grid, and $\boldsymbol{z_t}$ represents the needle insertion direction through the

template holes, as shown in Fig. 2(b). In the image coordinates, the 3D Euclidean distance represents the magnitude of the difference vector between the needle tips in the two modalities; however, in the template coordinate system, the difference vector between the needle tip position in 3D TRUS and CT was assessed in each of the coordinate directions. As the 3D Euclidean distance between the needle tips in the two modalities is preserved, each of the component values will be smaller than the total 3D Euclidean distance reported. In order to evaluate the magnitude of the errors in each of the template coordinate directions, the absolute value of each component was taken prior to calculating the mean and the mean absolute needle tip difference was reported for each direction.

2.D. *In vivo* study

Five patients undergoing HDR interstitial gynecologic brachytherapy at the London Health Sciences Centre provided written consent in accordance with the protocol approved by the Research Ethics Board at The University of Western Ontario (London, ON, Canada), as a proof-of-concept study. Three of the five patients were diagnosed with recurrent endometrioid adenocarcinoma of the uterus and the two remaining patients were diagnosed with squamous cell carcinoma of the vagina. All five patients were treated for vaginal masses using interstitial implants. The procedures were performed using stainless steel needles with a 0.5 mm solid tip and, for each patient, a 3D TRUS image was acquired following the insertion of all needles. Each scan was obtained with the vaginal cylinder of the perineal template approximately centered in the 3D image and all needle tips within the 3D image field-of-view, if possible. All US images were acquired with a depth setting of 6.4 cm. Following the 3D US scan, patients received the standard, clinical CT scan using a Philips Brilliance CT Big Bore Scanner (Philips Healthcare, Andover, MA, USA). Using our software, the 3D TRUS and CT images were manually, rigidly registered mainly based on the vaginal cylinder of the template. An additional point was used in the registration to orient the image around the cylinder, typically the location of a small hole at the end of the cylinder or other anatomical landmark, depending on the visible structures for each patient.

For both modalities, the tip of each needle was selected, if visible, as well as an additional point on the needle path. In order to assess the error introduced by the variability in locating a needle tip point, the fiducial localization error (FLE)[33,35] was determined for both modalities. This was performed using ten needles selected from the patient images to represent various positions relative to the template cylinder. The needle tips were identified in each modality five times with at least 24 h between selection sessions. The needle tip and secondary point on the needle path was used to calculate the needle trajectory difference and the 3D Euclidean distance between corresponding tips between the two modalities for each visible needle. If the needle in the US image extended beyond the image field-of-view or appeared to end at a much smaller depth than was clinically feasible, the needle tip was deemed not visible. Additionally, needle tips were considered not visible if the needle path was seen entering an artifact, such as a region of shadowing or air pocket, without clearly exiting the region obscured by the artifact. If the needle tip was not visible, the nearest distinguishable point on the needle path was selected for use in the needle trajectory calculation. All statistical analysis was performed using GraphPad Prism 7 (GraphPad Software, La Jolla, CA, USA).

The differences between visible corresponding needle tips in the 3D TRUS and CT images were also transformed into coordinates, (x_t, y_t, z_t), relative to the needle insertion template, as in the pelvic phantom study. In order to determine the rotation required for the transformation, the angle of the vaginal cylinder relative to the TRUS probe was determined using the registered CT image.

As the spatial resolution of the US transducer is not equivalent in every direction (axial, lateral, elevation),[25] the needle tip positions (for visible tips) were transformed into radial (r), tangential (t), and probe insertion (z) directions, as shown in Fig. 3(a), to reflect the differing spatial resolution in the radial and tangential directions due to the tilt acquisition method (see Fig. 4). This transformation was performed, as described in Hrinivich et al.,[36] such that the 3D Euclidean distance between needle tips in the two modalities is maintained. Thus, the x and y coordinates are transformed into the t and r coordinates, respectively, as demonstrated in Fig. 3(b), by rotating about the z axis. Principal component analysis (PCA) was performed with 95% prediction interval

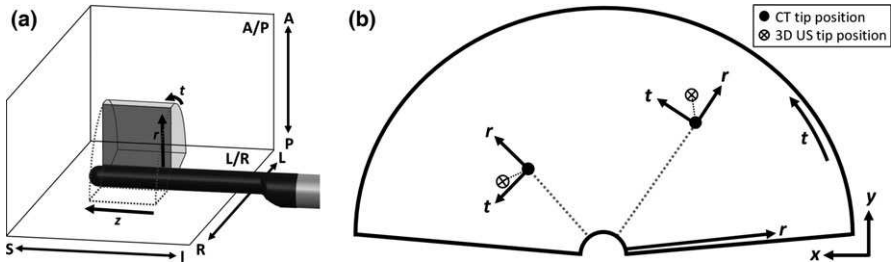

FIG. 3. (a) TRUS probe with r, t, and z directions and Anterior/Posterior (A/P) and Left/Right (L/R) planes indicated. (b) (x, y) plane of 3D TRUS scan, showing the relationship between x, y and r, t coordinates for example needle tips.

ellipses to determine the primary directions of tip error.[37] The trajectory differences were decomposed into the approximate Anterior/Posterior (A/P) and Left/Right (L/R) planes, as shown in Fig. 3(a). The Superior/Inferior (S/I) plane was omitted as needles are inserted almost perpendicular to this plane and therefore appear point-like in this plane.

3. RESULTS

3.A. Geometric phantom validation

Figure 4 shows the 3D US image of the grid phantom with the coordinate directions and expected values indicated. Table I summarizes the measurements made in each of the image planes. The mean error measurements in all directions in all planes ranged from 0.4% to 3.0% of the expected value.

A 3D US image of the volumetric phantom is shown in Fig. 5, showing the surface rendering of one of the tumor segmentations. The mean measured volume ± one standard deviation (SD) for the three segmentations of the tumor in the volumetric validation test was 46.67 ± 0.17 cm^3, which was within 0.2% of the expected volume (46.57 cm^3).

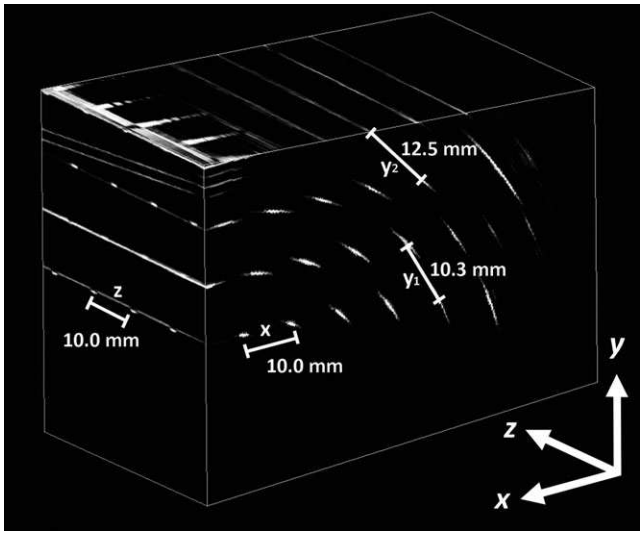

FIG. 4. 3D US image of the geometric grid phantom with coordinate planes and expected measurements indicated. The strings appear smeared in the (x, y) plane due to the differing spatial resolution in the radial and tangential directions.

TABLE I. Summary of distance measurements made in each of the three coordinate planes of the 3D US images.

	(x, y) plane			(x, z) plane		(y, z) plane		
	x	y_1	y_2	x	z	y_1	y_2	z
Expected distance (mm)	10.0	10.3	12.5	10.0	10.0	10.3	12.5	10.0
Mean distance (mm)	10.07	10.51	12.87	9.96	10.07	10.45	12.34	10.06
Standard deviation (mm)	0.15	0.23	0.25	0.15	0.09	0.24	0.24	0.08
Error (%)	0.7	2.0	3.0	0.4	0.7	1.4	1.3	0.6
N	20	12	12	28	12	8	8	16

3.B. Pelvic phantom study

Figure 6 shows the 3D US image and the registered MR image obtained from the pelvic phantom, with key features, including a fiducial rod, vaginal cylinder, and rectal canal, indicated and three needle paths visible. The mean angular needle trajectory difference ± SD between the two modalities was 0.94 ± 0.89 degrees and the mean Euclidean distance ± SD between needle tips was 1.54 ± 0.71 mm for the 14 needles. In the needle template coordinate system, (x_t, y_t, z_t), where z_t is the needle insertion direction, the mean absolute needle tip differences ± SD between the 3D US and MR images were 0.92 ± 0.43 mm, 0.93 ± 0.83 mm, and 0.42 ± 0.35 mm in the x_t, y_t, and z_t directions, respectively.

3.C. *In vivo* study

An example of a patient 3D US image is shown in Fig. 7 with landmark features highlighted. For the ten needles used, the FLE was 0.34 mm in the patient CT images and 1.55 mm in the patient 3D US images. For the five patients in the study, each patient had 14 to 16 needles placed for a total of 73 needles inserted. Of these needles, 64 needles (88%) were visible in the 3D TRUS images and 58 needle tips (79%) were identifiable. Of the nine needles that were not visible in the 3D TRUS images, six were not visible due to shadowing created by the presence of the template vaginal cylinder, as illustrated in Fig. 8. The additional three needles that were not visible were likely not visualized due to other artifacts, including artifacts due to remaining matter in the patients'

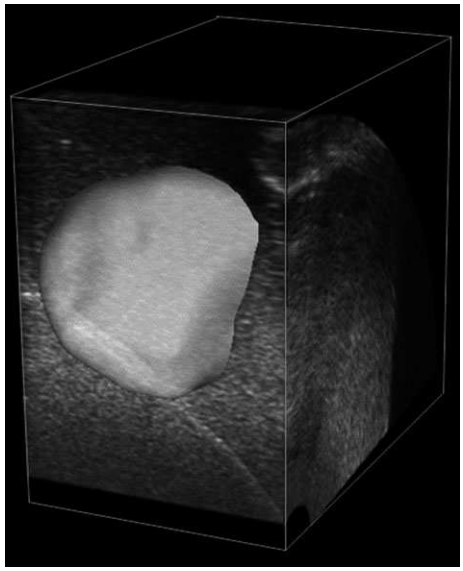

FIG. 5. 3D US image of the volumetric phantom showing the surface of the segmented tumor.

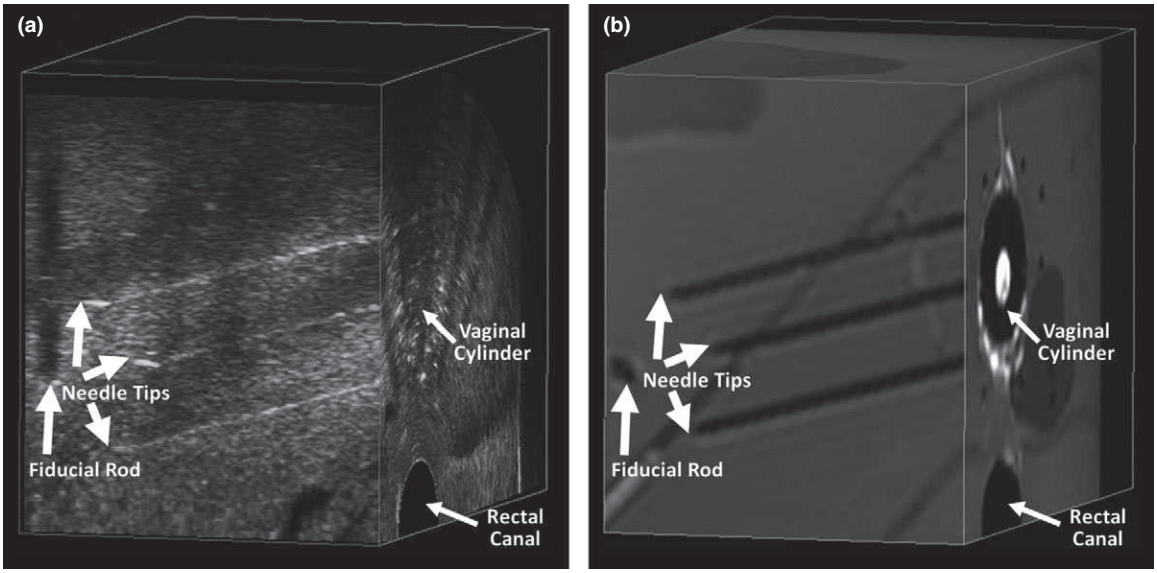

FIG. 6. (a) 3D TRUS phantom image with three needle tips, a fiducial rod, the vaginal cylinder, and rectal canal indicated. (b) The corresponding, registered MR phantom image, with key features indicated, including three needle tips, a fiducial rod, the vaginal cylinder, and rectal canal.

rectum at the time of imaging. Of the additional six needle tips that were not identifiable, three of these were due to the tips being outside of the field-of-view in the 3D TRUS images, as demonstrated in Fig. 9. The number of needles and needle tips visible, the mean difference in the needle trajectory between modalities, and the mean Euclidean distance between corresponding needle tips are summarized per patient in Table II. The mean trajectory difference ± SD between the two modalities was 3.04 ± 1.63 degrees for visible needles in the five patients and 76.6% of the 64 visible needles had differences less than 4 degrees, as shown in Fig. 10(a). The mean Euclidean distance ± SD between tips in the two modalities was 3.82 ± 1.86 mm for the 58 identifiable needle tips. The Euclidean distance between needle tip positions in the two modalities was less than 3 mm for 32.8% of visible needles tips and less than 5 mm for 70.7% of visible needle tips, as demonstrated in Fig. 10(b).

Table III summarizes the mean absolute needle tip differences between the 3D TRUS and corresponding, registered CT image for each patient in the needle template coordinate system, where z_t is the needle insertion direction. The mean absolute tip differences ± SD for the visible needle tips in the x_t, y_t, and z_t directions were 2.32 ± 1.78 mm, 1.80 ± 1.44 mm, and 1.49 ± 1.44 mm, respectively. Patient D had the largest mean absolute difference in the insertion direction, z_t, of 1.92 ± 2.03 mm.

Figure 11(a) shows the 3D needle tip differences in the radial, tangential, and probe insertion axis (r, t, z) coordinate system, the projections of the needle tip differences onto the 2D planes, and the 95% prediction interval ellipses (containing 95% of the points) derived from the PCA. The centroid of the distribution is at (r, t, z) = (1.14 mm, 0.57 mm, −0.39 mm), indicating a small bias in the radial (r) component. This may have resulted from needles shifting away from the TRUS probe surface due to the probe pressure on the rectal wall, as illustrated in Fig. 12, showing a patient 3D TRUS image with a shifted needle and the corresponding CT image. The mean absolute tip differences ± SD for the visible tips in the r, t, and z directions were 1.89 ± 1.74 mm, 2.46 ± 1.70 mm, and 1.53 ± 1.39 mm, respectively, showing the largest differences in the tangential direction (t) due to the reduced spatial resolution. To highlight the radial bias and the effect of the spatial resolution, the tip difference projections and corresponding 95% prediction interval ellipse is shown in the (r, t) plane in Fig. 11(b). Figure 13 shows the trajectory differences between the two modalities in the approximate A/P and L/R planes for each patient. The mean trajectory difference ± SD for visible needles in all patients

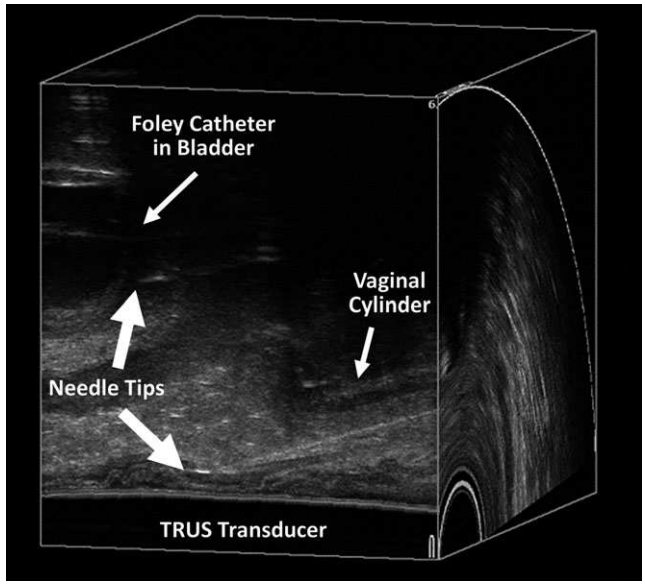

FIG. 7. Patient 3D US image with the position of the TRUS transducer, vaginal cylinder of the perineal template, Foley catheter in the bladder, and two needle tips indicated.

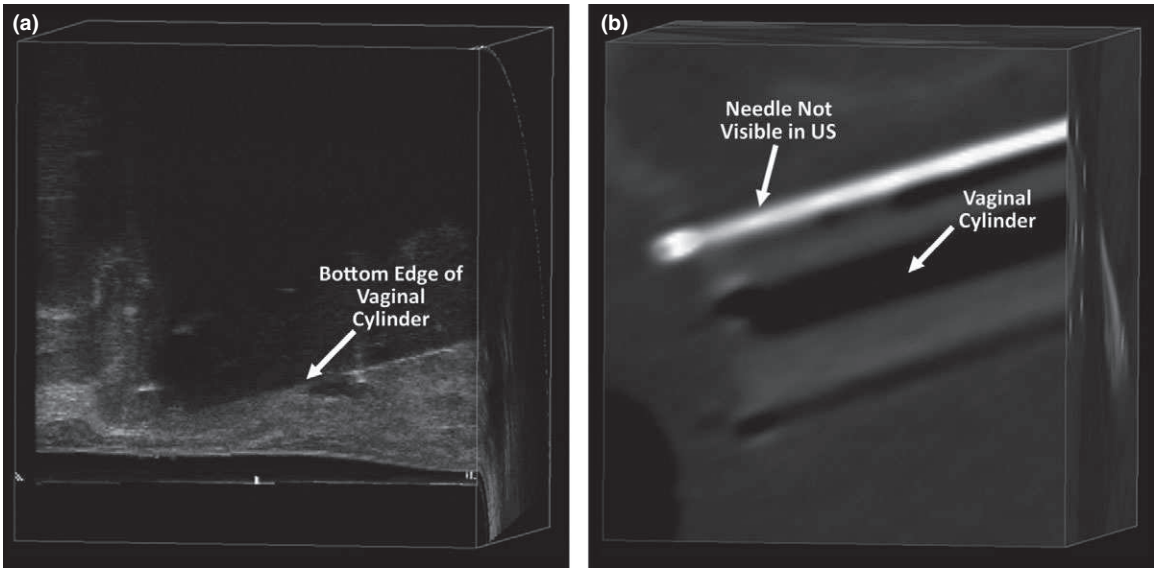

FIG. 8. (a) 3D TRUS patient image showing shadowing created on the anterior side of the vaginal cylinder of the perineal template, with the bottom edge (posterior side) of the vaginal cylinder indicated. (b) The corresponding, registered CT scan, showing the vaginal cylinder and a needle not visible in the 3D TRUS scan due to the shadowing artifact.

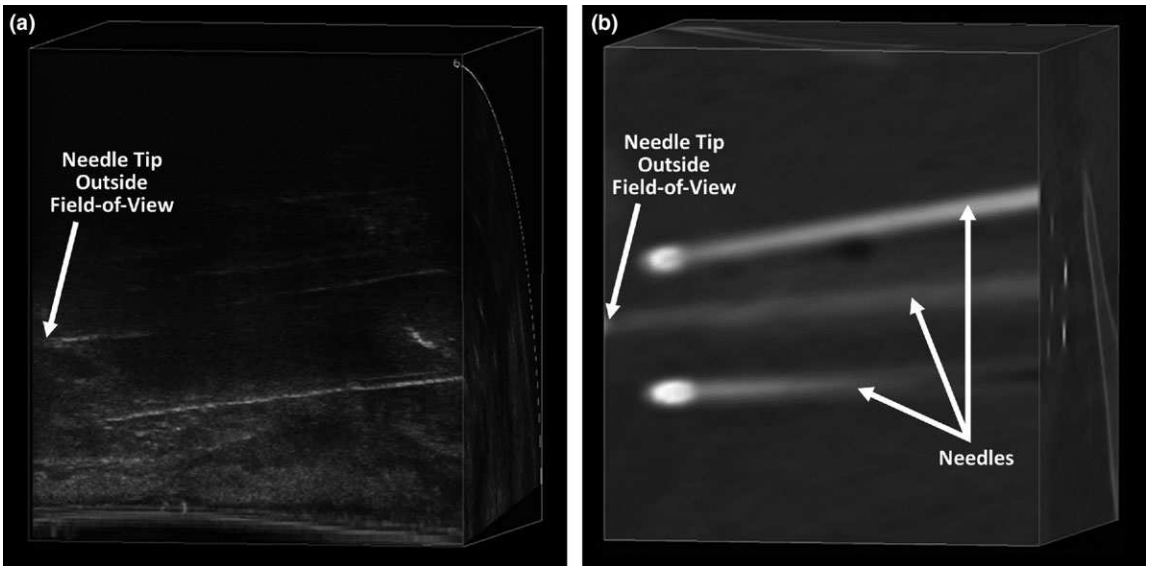

FIG. 9. (a) 3D TRUS patient image showing the centermost needle extending beyond the image field-of-view, making the needle tip unidentifiable. (b) The corresponding, registered CT scan, showing the centermost needle tip extending beyond the image field-of-view.

TABLE II. Mean needle trajectory differences and mean Euclidean difference in needle tip position between the 3D TRUS image and registered CT image for each patient. Of the total 73 needles placed, 88% were visible and 79% of needle tips were visible.

Patient ID	Number of needles placed	Number of needles visible	Number of needle tips visible	Mean trajectory difference ± SD (degrees)	Mean tip position difference ± SD (mm)
A	14	14	14	2.15 ± 1.28	3.90 ± 2.08
B	14	13	13	3.89 ± 1.86	4.28 ± 1.90
C	15	11	10	3.53 ± 1.81	2.87 ± 1.64
D	16	14	10	3.44 ± 1.20	4.38 ± 1.84
E	14	12	11	2.26 ± 1.37	3.54 ± 1.67
Overall	73	64	58	3.04 ± 1.63	3.82 ± 1.86

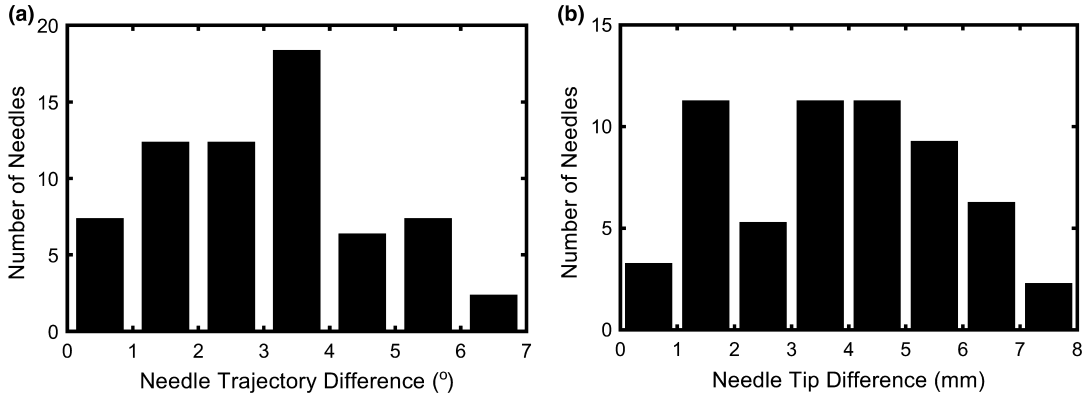

FIG. 10. (a) Histogram of patient needle trajectory differences between the 3D TRUS and corresponding, registered CT for the 64 visible needles. (b) Histogram of patient needle tip differences between the 3D TRUS and corresponding, registered CT positions for the 58 visible needle tips.

TABLE III. Mean absolute needle tip differences between the 3D TRUS image and registered CT image for each patient in the needle template coordinate system, (x_t, y_t, z_t), such that z_t is the insertion direction of the needles.

Patient ID	Difference in $x_t \pm$ SD (mm)	Difference in $y_t \pm$ SD (mm)	Difference in $z_t \pm$ SD (mm)
A	2.80 ± 2.18	1.59 ± 1.10	1.33 ± 1.33
B	2.50 ± 1.56	2.31 ± 1.86	1.52 ± 1.36
C	1.27 ± 0.88	1.35 ± 0.95	1.85 ± 1.42
D	2.15 ± 1.41	2.37 ± 1.43	1.92 ± 2.03
E	2.74 ± 2.04	1.22 ± 1.05	0.88 ± 0.74
Overall	2.32 ± 1.78	1.80 ± 1.44	1.49 ± 1.44

in the A/P plane was 0.89 ± 2.52 degrees and in the L/R plane was 0.04 ± 2.28 degrees.

4. DISCUSSION

This study evaluated a 3D side-fire TRUS system for intra-operative needle visualization during HDR interstitial gynecologic brachytherapy. While the use of 2D side-fire TRUS has been reported,[13–15] to the authors' knowledge, this is the first 3D TRUS system to be investigated for use during HDR interstitial gynecologic brachytherapy, incorporating the benefits associated with 3D image-guidance. The system has observed geometric errors of ≤ 0.3 mm in each of the three coordinate planes of the 3D US image and mean measured volumetric errors of 0.10 cm^3. We have shown that our 3D US system can accurately measure the positions of needles within the field-of-view that are not obscured by artifacts in both phantom and patient studies.

The phantom study using the female pelvic phantom produced a mean 3D Euclidean distance between corresponding needle tips of 1.54 ± 0.71 mm for the 14 needles placed, which is comparable to the mean tip error of 1.7 ± 0.5 mm for 15 needles reported for a phantom study using an active MR tracking system by Wang et al.[21] The mean tip position difference in the pelvic phantom is comparable to the voxel dimensions of the MR image, as these images were acquired with a voxel size of 1.17 × 1.17 × 1.20 mm^3 (voxel size of the 3D US images was 0.144 × 0.145 × 0.145 mm^3), and may be partially attributed to the uncertainty introduced by the image voxel size. The phantom study performed in our investigation was limited by the use of MR images as the ground truth by which to assess the needle positions identified in 3D TRUS, as MR is not commonly used to assess needle positions clinically. Additionally, stainless steel needles were used in the phantom study in order to mimic the standard clinical practice at our institution and assess their visibility under 3D US imaging. Consequently, the needles were removed prior to MR imaging and therefore the US needle positions could only be compared to the needle tracks. This possibly produced small deformations from the true needle position, particularly at the needle tip. MR was chosen over comparison to CT, as needles generated artifacts in the phantom CT images and needle tracks were not clearly visible in CT. The expected needle positions were not used for comparison, as this would not account for any needle deflections in the phantom. The MR images, however, clearly showed the needle paths and fiducials and were sufficient for assessing the feasibility of using 3D TRUS for visualizing the needles during this procedure.

For the patient study, the mean Euclidean distance ± SD between corresponding needle tips in 3D TRUS and CT was 3.82 ± 1.86 mm with 32.8% of identifiable needles having differences less than 3 mm and 70.7% of identifiable needles having differences less than 5 mm for the total of 58 identifiable needles used in five patients. This is comparable to values reported by Hrinivich et al.,[38] when comparing 2D and 3D TRUS for visualizing needles during HDR prostate brachytherapy, reporting tip differences of less than 3 mm for 33% of needles and less than 5 mm for 64% of needles in a study of 12 patients undergoing a similar imaging procedure and evaluating 183 needles. In the needle template coordinates, the direction with the lowest mean absolute difference was the needle insertion direction with a maximum over all patients of 1.92 ± 2.03 mm (Patient D), but had the greatest variability during treatment since the other two directions are physically constrained by the template. Given this greater uncertainty associated with needle placement in the needle insertion direction, it is clinically important to have accurate

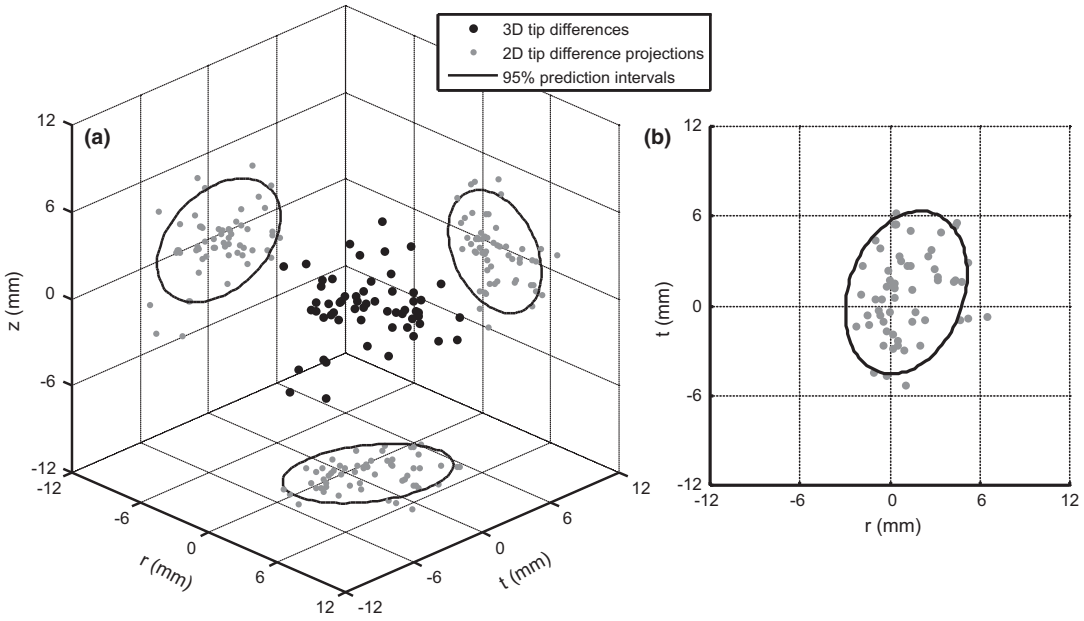

FIG. 11. (a) Needle tip differences between the 3D TRUS image and corresponding CT scan in the radial (***r***), tangential (***t***), and probe insertion (***z***) directions, showing the projections of the needle tip differences onto the 2D planes and the 95% prediction interval ellipses. (b) (***r***, ***t***) plane showing the projected 2D needle tip position differences and corresponding 95% prediction interval ellipse, highlighting a bias in the positive radial direction and the larger differences in the tangential direction.

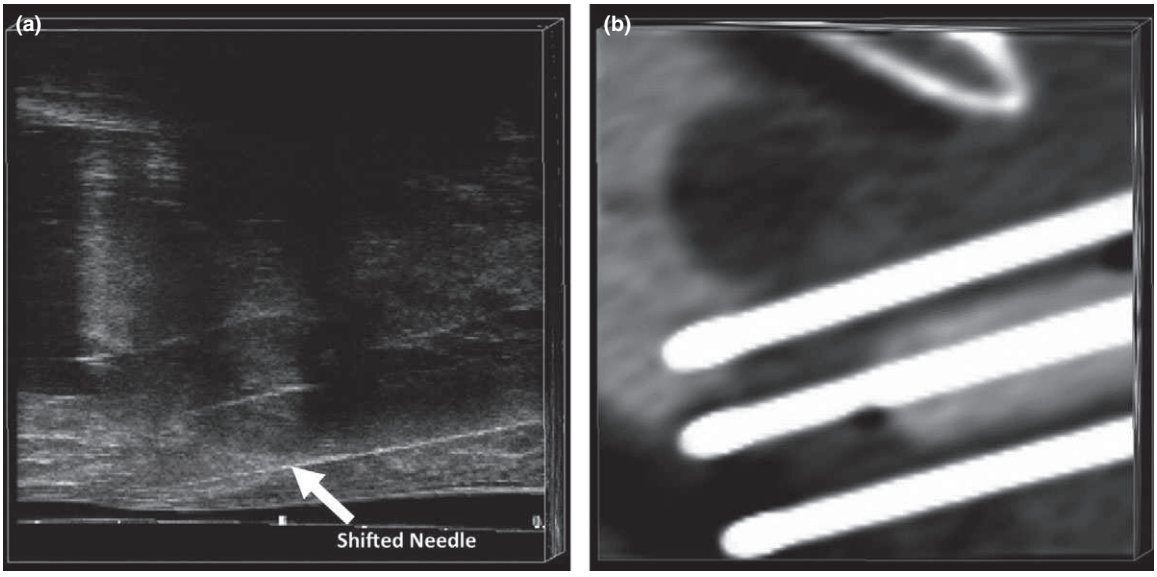

FIG. 12. (a) 3D TRUS patient image with needle shifted anteriorly due to probe pressure indicated. (b) Rigidly registered patient CT image showing the bottommost needle in the unshifted position.

needle localization in this direction. As the 3D TRUS system showed the lowest difference between modalities in the insertion direction, it has the potential to reduce the uncertainty in needle positioning in this direction, intra-operatively. Additionally, the needle positions, particularly in the $\boldsymbol{x_t}$ and $\boldsymbol{y_t}$ directions, are potentially affected by differences in patient configuration between the time of the 3D TRUS and CT image acquisition. Specifically, patient position, including lowering the patients' legs from the lithotomy position used for needle insertion, the presence of the US probe in the rectum, changes in tissues, and the degree of bladder filling[39] may have contributed to the larger differences in the needle positions in the $\boldsymbol{x_t}$ and $\boldsymbol{y_t}$ directions between the 3D TRUS and CT imaging, which is a limitation of this study.

A typical step size for radiation source dwell positions during this treatment is 5 mm[6] using a 4.52 mm long encapsulated HDR Iridium-192 source.[40] The difference between modalities in the needle insertion direction will affect the placement of these dwell positions along the needle path and error in the needle tip position can create uncertainty in

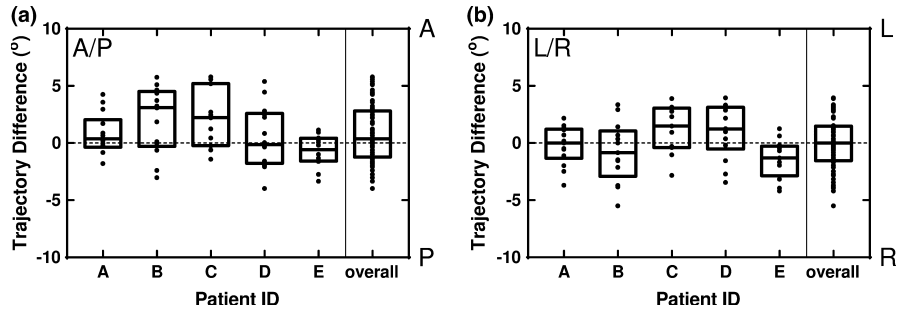

FIG. 13. (a) Needle trajectory difference between the 3D TRUS and CT images in the Anterior/Posterior (A/P) plane for each patient and overall. (b) Needle trajectory difference between the 3D TRUS and CT images in the Left/Right (L/R) plane for each patient and overall.

coverage, particularly the superior dose coverage. The dwell positions for the radioactive source depend on both the needle tip position and the needle trajectory. The differences observed in the needle positions in each of the coordinate directions could influence the dose coverage and the impact of these differences should be investigated. The dosimetric impact of the differences is also influenced by the uncertainty in the size and position of the target contour and the relative positions of the OAR. Additionally, the errors associated with needles must be evaluated in the context of their position on the template, as differences in central needles tend to have less of an impact on the dose coverage in comparison to peripheral needles. Due to the compounding and compensating effects resulting from the placement of multiple needles, a comprehensive future simulation study, such as the study conducted for low-dose-rate prostate brachytherapy by Lindsay et al.,[41] will be carried out with a larger sample size to determine the effect of the tip and trajectory differences on the treatment plan. The dosimetric consequences resulting from these differences will be assessed in this future study, including variations in target coverage and volumes receiving higher or lower dose than in the CT-based plan.

Evaluating the needle tip differences seen in this study in the radial, tangential, and probe insertion (r, t, z) coordinate system, showed a small bias in the positive radial direction (away from the US probe). This was likely a result of the pressure exerted by the US probe on the rectal wall creating a shift away from the probe, which is not present during the CT image acquisition, resulting in a difference in needle tip position. These differences, potentially due to probe pressure, are also observed in the trajectory differences, which showed a slight bias in the anterior direction, approximately corresponding to the radial direction for needles placed near the rectal wall. This type of needle shift was most apparent in Patients B and C, as can be seen in Fig. 13(a), and these cases also showed the largest mean trajectory differences of 3.89 ± 1.86 degrees and 3.53 ± 1.81 degrees, respectively. Additionally, evaluation of the needle tip differences in the (r, t, z) coordinate system showed the largest needle tip differences in the tangential (t) direction due to the reduced spatial resolution resulting from the tilt acquisition method.[24,25] This is visually demonstrated in Fig. 4, as it can be seen that the strings appear smeared in the tangential direction, creating difficulty when identifying the strings and needles in both phantom and patient studies.

One limitation of this study is the registration step between the 3D TRUS and CT images in order to assess the positions of the needles in the US images. Due to the lack of anatomical features visible in US images, as well as the lack of fixed structures between the 3D TRUS and CT acquisitions, the two modalities were manually registered mainly based on the position of the vaginal cylinder of the needle template, as it is the most identifiable, rigid structure in both modalities. The registration between the two modalities introduces some inherent error, particularly due to deformations with time and patient position, contributing to the differences recorded in the needle positions between 3D TRUS and CT images. An additional limitation of this investigation is that all procedures were performed using stainless steel needles and therefore the results of this study may be different if an alternate type of needle, such as plastic needles, was used, as is the practice at some other institutions.

The main limitation of the 3D TRUS approach demonstrated in this study is a shadowing artifact created by the vaginal cylinder of the needle template. Of the 73 needles placed in the five patients, nine needles were not identifiable in the 3D TRUS images and six of these were due to the vaginal cylinder artifact. This shadow obscures needles placed on the anterior side of the vaginal cylinder. This may be mitigated in the future by investigating an alternate material for the vaginal cylinder. Alternatively, the effect of this artifact may be minimized by inserting the anterior needles first, acquiring an intermediate scan, then inserting the vaginal cylinder and remaining needles prior to a postinsertion 3D US. In some cases, 2D transvaginal US (TVUS) is currently used to visualize anterior needles prior to insertion of the vaginal cylinder,[42] and thus a TVUS approach may be suitable for an intermediate scan to visualize the anterior needles' placement before the cylinder is introduced. Three additional needle tips were not identified in the 3D US image, as they were outside the US field-of-view; however, these needle tips may have been visible with a deeper probe insertion, and this limitation may be overcome with greater operator experience. In this study, the needles placed did not extend far beyond the end of the vaginal cylinder and, therefore, it is not known if this technique would be appropriate for visualizing needle

tips within the field-of-view in cases requiring larger insertion depths. The further three needles and additional three needle tips that were not visible were likely due to other artifacts, including shadowing from other needles and remaining matter in the rectum. Visualization may be improved by introducing a preparation procedure to cleanse remaining matter from the rectum prior to US imaging. This may also allow for adequate coupling to be achieved between the rectal wall and the US probe with less pressure, reducing the resulting needle shifting. Nevertheless, the 3D TRUS system provided intra-operative visualization of 88% of needles placed and 79% of needle tips during HDR interstitial gynecologic brachytherapy and provides the benefits of 3D image-guidance. The 3D TRUS system uses a conventional 2D TRUS probe, thereby reducing the need for specialized equipment compared to the typical requirements for 3D imaging, and allowing for the system to be used with minimal set-up time. As the 3D TRUS system requires only 12 s to acquire an image, its use does not substantially increase the time required for the needle insertion procedure. The increased certainty in needle positioning intra-operatively, possibly enabling fewer needles to be inserted, may also shorten the procedure time. Improved 3D guidance systems, including 3D TRUS, provide the potential to reduce procedure times and allow for needle placement tailored to a patient's specific tumor with potentially fewer needles placed.

5. CONCLUSION

The 3D TRUS system provides a method for visualizing needles intra-operatively during HDR interstitial brachytherapy of gynecologic cancers. In this proof-of-concept study, the 3D TRUS system allowed for localization of needles not obscured by shadowing artifacts, providing the advantages of 3D imaging and the potential for intra-operative 3D image-guidance.

ACKNOWLEDGMENTS

The authors gratefully acknowledge funding from the Ontario Institute of Cancer Research. J. Rodgers was supported by the Natural Sciences and Engineering Research Council (NSERC) of Canada, the Cancer Research and Technology Transfer Strategic Training Program (CaRTT), and the Ontario Graduate Scholar (OGS) Program. Many thanks to Dr. David Tessier for helping with experiments, Lori Gardi for software development, and Jacques Montreuil and Kevin Barker for lending their fabrication talents.

CONFLICTS OF INTEREST

The authors have no relevant conflicts of interest to disclose.

[a)]Author to whom correspondence should be addressed. Electronic mail: jrodge23@uwo.ca.

REFERENCES

1. Stewart BW, Wild CP, eds. *World Cancer Report 2014*. World Health Organization; 2014.
2. Viswanathan AN, Thomadsen B, American Brachytherapy Society Cervical Cancer Recommendations Committee. American Brachytherapy Society consensus guidelines for locally advanced carcinoma of the cervix. Part I: general principles. *Brachytherapy.* 2012;11:33–46.
3. Viswanathan AN, Erickson BE, Rownd J. Image-Based Approaches to Interstitial Brachytherapy. In: Viswanathan AN, Kirisits C, Erickson BE, Pötter R, eds. *Gynecol. Radiat. Ther. Nov. Approaches to Image-Guidance Manag*. Berlin Heidelberg: Springer-Verlag; 2011:247–259.
4. Haie-Meder C, Gerbaulet A, Pötter R. Interstitial brachytherapy in gynaecological cancer. In: Gerbaulet A, Pötter R, Mazeron J-J, Meertens H, Van Limbergen E, eds. *GEC ESTRO Handb. Brachytherapy.* Brussels: European Society for Therapeutic Radiology and Oncology (ESTRO); 2002: 417–433.
5. Martinez A, Edmundston GK, Cox RS, Gunderson LL, Howes AE. Combination of external beam irradiation and multiple-site perineal applicator (MUPIT) for treatment of locally advanced or recurrent prostatic, anorectal, and gynecologic malignancies. *Int J Radiat Oncol Biol Phys*. 1985;11:391–398.
6. D'Souza D, Wiebe E, Patil N, et al. CT-based interstitial brachytherapy in advanced gynecologic malignancies: outcomes from a single institution experience. *Brachytherapy.* 2014;13:225–232.
7. Viswanathan AN, Moughan J, Small W Jr, et al. The quality of cervical cancer brachytherapy implantation and the impact on local recurrence and disease-free survival in radiation therapy oncology group prospective trials 0116 and 0128. *Int J Gynecol Cancer.* 2012;22:123–131.
8. Scanlan KA, Propeck PA, Lee FT. Invasive procedures in the female pelvis: value of transabdominal, endovaginal, and endorectal US guidance. *Radiographics*. 2001;21:491–506.
9. Nag S, Martínez-Monge R, Ellis R, et al. The use of fluoroscopy to guide needle placement in interstitial gynecological brachytherapy. *Int J Radiat Oncol Biol Phys*. 1998;40:415–420.
10. Eisbruch A, Johnston CM, Martel MK, et al. Customized gynecologic interstitial implants: CT-based planning, dose evaluation, and optimization aided by laparotomy. *Int J Radiat Oncol Biol Phys*. 1998;40:1087–1093.
11. Corn BW, Lanciano RM, Rosenblum N, Schnall M, King S, Epperson R. Improved treatment planning for the Syed-Neblett template using endorectal-coil magnetic resonance and intraoperative (Laparotomy/Laparoscopy) guidance: a new integrated technique for hysterectomized women with vaginal tumors. *Gynecol Oncol*. 1995;56:255–261.
12. Choi JC, Ingenito AC, Nanda RK, et al. Potential decreased morbidity of interstitial brachytherapy for gynecologic malignancies using laparoscopy: a pilot study. *Gynecol Oncol*. 1999;73:210–215.
13. Stock RG, Chan K, Terk M, Dewyngaert JK, Stone NN, Dottino P. A new technique for performing Syed-Neblett template interstitial implants for gynecologic malignancies using transrectal-ultrasound guidance. *Int J Radiat Oncol Biol Phys*. 1997;37:819–825.
14. Sharma DN, Rath GK, Thulkar S, Kumar S, Subramani V, Julka PK. Use of transrectal ultrasound for high dose rate interstitial brachytherapy for patients of carcinoma of uterine cervix. *J Gynecol Oncol*. 2010;21:12–17.
15. Weitmann HD, Knocke TH, Waldhäusl C, Pötter R. Ultrasound-guided interstitial brachytherapy in the treatment of advanced vaginal recurrences from cervical and endometrial carcinoma. *Strahlentherapie und Onkol*. 2006;182:86–95.
16. Erickson BA, Foley WD, Gillin M, Albano K, Wilson JF. Ultrasound-guided transperineal interstitial implantation of gynecologic malignancies: description of the technique. *Endocurietherapy/Hyperthermia Oncol*. 1995;11:107–113.
17. Rodgers J, Tessier D, D'Souza D, Leung E, Hajdok G, Fenster A. Development of 3D ultrasound needle guidance for high-dose-rate interstitial brachytherapy of gynaecological cancers. *Proc SPIE Med Imaging*. 2016;9790:97900I.
18. Lee LJ, Damato AL, Viswanathan AN. Clinical outcomes of high-dose-rate interstitial gynecologic brachytherapy using real-time CT guidance. *Brachytherapy.* 2013;12:303–310.
19. Viswanathan AN, Szymonifka J, Tempany-Afdhal CM, O'Farrell DA, Cormack RA. A prospective trial of real-time magnetic resonance-guided

catheter placement in interstitial gynecologic brachytherapy. *Brachytherapy*. 2013;12:240–247.
20. Kapur T, Egger J, Damato A, Schmidt EJ, Viswanathan AN. 3T MR-guided brachytherapy for gynecologic malignancies. *Magn Reson Imaging*. 2012;30:1279–1290.
21. Wang W, Viswanathan AN, Damato AL, et al. Evaluation of an active magnetic resonance tracking system for interstitial brachytherapy. *Med Phys*. 2015;42:7114–7121.
22. Viswanathan AN, Cormack R, Holloway CL, et al. Magnetic resonance-guided interstitial therapy for vaginal recurrence of endometrial cancer. *Int J Radiat Oncol Biol Phys*. 2006;66:91–99.
23. Kamrava M. Potential role of ultrasound imaging in interstitial image based cervical cancer brachytherapy. *J Contemp Brachytherapy*. 2014;6:223–30.
24. Fenster A, Downey DB, Cardinal HN. Three-dimensional ultrasound imaging. *Phys Med Biol*. 2001;46:R67–R99.
25. Fenster A, Downey DB. Three-dimensional ultrasound imaging. *Annu Rev Biomed Eng*. 2000;2:457–475.
26. Tong S, Downey DB, Cardinal HN, Fenster A. A three-dimensional ultrasound prostate imaging system. *Ultrasound Med Biol*. 1996;22:735–46.
27. Fenster A, Dunne S, Chan TKC, Downey D. *Method and system for constructing and displaying three-dimensional images*. U.S. Patent No. 5,454,371; 1995.
28. Downey D, Fenster A, Miller J, Tong S. *Three dimensional ultrasound imaging system*. U.S. Patent No. 5,562,095; 1996.
29. Fenster A, Dunne S, Larsen JT. *Three-dimensional imaging system*. U.S. Patent No. 5,842,473; 1998.
30. Rickey DW, Picot PA, Christopher DA, Fenster A. A wall-less vessel phantom for Doppler ultrasound studies. *Ultrasound Med Biol*. 1995;21:1163–1176.
31. Kishimoto J, deRibaupierre S, Lee DSC, Mehta R, St Lawrence K, Fenster A. 3D ultrasound system to investigate intraventricular hemorrhage in preterm neonates. *Phys Med Biol*. 2013;58:7513–7526.
32. Cool D, Sherebrin S, Izawa J, Chin J, Fenster A. Design and evaluation of a 3D transrectal ultrasound prostate biopsy system. *Med Phys*. 2008;35:4695–4707.
33. Fitzpatrick JM, Hill DLG, Maurer CR Jr. Image registration. In: Sonka M, Fitzpatrick JM, eds. *Handbook of Medical Imaging: Volume 2. Medical Image Processing and Analysis*. Bellingham, WA: SPIE Press; 2000: 447–514.
34. Williams G. *Linear Algebra With Applications*, 6th ed. Sudbury, MA: Jones & Bartlett Learning; 2007.
35. Fitzpatrick JM, West JB, Maurer CR Jr. Predicting error in rigid-body point-based registration. *IEEE Trans Med Imaging*. 1998;17:694–702.
36. Hrinivich WT, Hoover DA, Surry K, et al. Simultaneous automatic segmentation of multiple needles using 3D ultrasound for high-dose-rate prostate brachytherapy. *Med Phys*. 2017. doi: 10.1002/mp.12148. [Epub ahead of print].
37. Irwin MR, Downey DB, Gardi L, Fenster A. Registered 3-D ultrasound and digital stereotactic mammography for breast biopsy guidance. *IEEE Trans Med Imaging*. 2008;27:391–401.
38. Hrinivich WT, Hoover DA, Surry K, et al. Three-dimensional transrectal ultrasound guided high-dose-rate prostate brachytherapy: a comparison of needle segmentation accuracy with two-dimensional image guidance. *Brachytherapy*. 2016;15:231–239.
39. Damato AL, Cormack RA, Viswanathan AN. Characterization of implant displacement and deformation in gynecologic interstitial brachytherapy. *Brachytherapy*. 2014;13:100–109.
40. Varian Medical Systems *GammaMedplus iX, 3/24 iX afterloaders feature sheet*, 2014.
41. Lindsay PE, Van Dyk J, Battista JJ. A systematic study of imaging uncertainties and their impact on ^{125}I prostate brachytherapy dose evaluation. *Med Phys*. 2003;30:1897–1908.
42. Viswanathan AN, Erickson BA. Seeing is saving: the benefit of 3D imaging in gynecologic brachytherapy. *Gynecol Oncol*. 2015;138:207–215.